

**NASA**

**Technical**

**Paper**

**2945**

**November 1989**

# Low-Speed, High-Lift Aerodynamic Characteristics of Slender, Hypersonic Accelerator-Type Configurations

Gregory M. Gatlin

(NASA-TP-2945) LOW-SPEED, HIGH-LIFT  
AERODYNAMIC CHARACTERISTICS OF SLENDER,  
HYPERSONIC ACCELERATOR-TYPE CONFIGURATIONS  
(NASA) 45 p

CSCL 01A

N90-10830

Unclas

H1/02 0224543

**NASA**

Date	Description
1998-01-01	Initial deposit
1998-01-15	Withdrawal
1998-02-01	Interest
1998-02-15	Withdrawal
1998-03-01	Interest
1998-03-15	Withdrawal
1998-04-01	Interest
1998-04-15	Withdrawal
1998-05-01	Interest
1998-05-15	Withdrawal
1998-06-01	Interest
1998-06-15	Withdrawal
1998-07-01	Interest
1998-07-15	Withdrawal
1998-08-01	Interest
1998-08-15	Withdrawal
1998-09-01	Interest
1998-09-15	Withdrawal
1998-10-01	Interest
1998-10-15	Withdrawal
1998-11-01	Interest
1998-11-15	Withdrawal
1998-12-01	Interest
1998-12-15	Withdrawal
1999-01-01	Interest
1999-01-15	Withdrawal
1999-02-01	Interest
1999-02-15	Withdrawal
1999-03-01	Interest
1999-03-15	Withdrawal
1999-04-01	Interest
1999-04-15	Withdrawal

**NASA  
Technical  
Paper  
2945**

1989

Low-Speed, High-Lift  
Aerodynamic  
Characteristics of  
Slender, Hypersonic  
Accelerator-Type  
Configurations

Gregory M. Gatlin  
*Langley Research Center  
Hampton, Virginia*

**NASA**

National Aeronautics and  
Space Administration  
Office of Management  
Scientific and Technical  
Information Division



## Summary

Two investigations were conducted in the Langley 14- by 22-Foot Subsonic Tunnel to determine the low-speed aerodynamic characteristics of a generic hypersonic accelerator-type configuration. The model was a delta wing configuration incorporating a conical forebody, a simulated wrap-around engine package, and a truncated conical afterbody. Six-component force and moment data were obtained over a range of angle of attack from  $-4^\circ$  to  $30^\circ$  and a range of sideslip angle from  $-20^\circ$  to  $20^\circ$ . In addition to tests of the basic configuration, component buildup tests were conducted, and the effects of power, forebody nose geometry, canard surfaces, fuselage strakes, and engines on the lower surface alone were also determined. Control power available from deflections of wing flaps and afterbody flaps in the exhaust flow was also investigated. Surface pressure data were obtained at several longitudinal locations along the conical forebody. Surface oil flows and smoke flow visualization with the use of a laser light sheet were used for diagnostic analysis of the flow over the model and as an aid in the interpretation of the force and moment data.

The high-fineness-ratio conical forebody had a significant effect on the behavior of the configuration aerodynamics. At the moderate angles of attack associated with takeoff and landing conditions, vortex flow from the conical forebody created large values of local inflow angles at the engine inlet locations on the leeward side of the model. In addition, large yawing moments resulted from asymmetric flow fields exhibited by the forebody. Increasing nose bluntness reduced the yawing-moment asymmetry, and the addition of a canard eliminated the yawing-moment asymmetry. The control power available from afterbody flap deflections was significantly increased during power-on conditions.

## Introduction

Due in part to the National Aero-Space Plane Program there has been renewed interest in hypersonic flight with particular emphasis on single stage to orbit and the ability to operate with a horizontal takeoff and landing. These current design requirements have resulted in several unique, new configurations such as the accelerator incorporating a slender conical shape for low drag and a highly swept delta wing. Little is currently known about the low-speed aerodynamics of such configurations in the takeoff and landing regime; therefore, efforts are now underway to develop the data base needed for the design of these advanced vehicles.

As noted in reference 1, approach and takeoff speeds of these configurations will be determined by maximum lift coefficients available in the angle-of-attack range from  $10^\circ$  to  $15^\circ$ . For such slender, conical configurations, references 2 and 3 show that yawing moments will develop at zero sideslip as the angle of attack exceeds a value of approximately twice the semiapex angle. In the present study this angle of attack may be as low as  $10^\circ$  to  $12^\circ$ , well within the expected operational range for takeoff and approach. Therefore, the present study focused carefully on an examination of the lateral-directional characteristics of the configuration and on the dual objectives of providing techniques for minimizing deleterious directional effects and providing sufficient control power to trim the configuration.

This paper presents highlights of two investigations conducted in the Langley 14- by 22-Foot Subsonic Tunnel to study the low-speed aerodynamics of a generic hypersonic accelerator-type configuration. The primary features of the configuration are a slender conical forebody, a delta wing planform, a simulated wrap-around engine package, and a truncated conical afterbody. The first study was conducted with a  $6^\circ$  conical forebody to investigate the basic aerodynamics and flow field with and without power effects. The second wind-tunnel test used a  $5^\circ$  conical forebody and investigated control concepts designed to take advantage of dominant flow fields observed in the first entry. In addition, detailed surface pressure data were obtained on the  $5^\circ$  conical forebody in order to better define the influence of the strong vortical flows. Both powered and unpowered tests were conducted for both configurations. An angle-of-attack range from  $-4^\circ$  to  $30^\circ$  and a sideslip range from  $-20^\circ$  to  $20^\circ$  was covered. Most of the tests were conducted at a Reynolds number per foot of  $1.29 \times 10^6$ . Data obtained included six-component force and moment data, forebody surface pressures, and on-surface and off-surface flow visualization.

## Symbols

All measurements were made in and are presented in U.S. Customary Units. All data have been reduced to standard coefficient form, and longitudinal data are presented in the stability axis system while yawing-moment and side-force data are presented in the body axis system. The moment reference center was located at 62 percent of the fuselage length for both investigations.

$b$	wing span, ft
BL	buttock line, in.
$\bar{c}$	wing mean geometric chord, ft

$C_A$	axial-force coefficient, $\frac{\text{Axial force}}{q_\infty S}$
$C_D$	drag coefficient, $\frac{\text{Drag}}{q_\infty S}$
$C_L$	lift coefficient, $\frac{\text{Lift}}{q_\infty S}$
$C_m$	pitching-moment coefficient, $\frac{\text{Pitching moment}}{q_\infty S \bar{c}}$
$C_n$	yawing-moment coefficient, $\frac{\text{Yawing moment}}{q_\infty S b}$
$C_{n_\beta}$	weathercock stability derivative, $\frac{\partial C_n}{\partial \beta}$
$C_N$	normal-force coefficient, $\frac{\text{Normal force}}{q_\infty S}$
$C_p$	pressure coefficient, $\frac{p_{s,\text{local}} - p_\infty}{q_\infty}$
$C_T$	thrust coefficient, $\frac{\text{Static thrust}}{q_\infty S}$
$C_Y$	side-force coefficient, $\frac{\text{Side force}}{q_\infty S}$
FS	fuselage station, in.
$p_{s,\text{local}}$	pressure measured at local static-pressure orifice, psf
$p_\infty$	free-stream static pressure, psf
$q_\infty$	free-stream dynamic pressure, $\frac{1}{2} \rho V^2$ , psf
$r_N$	nose tip radius as a percent of forebody length
$S$	wing area, ft <sup>2</sup>
$V$	velocity, ft/sec
$\alpha$	angle of attack, deg
$\beta$	sideslip angle, deg
$\delta_{\text{ABF}}$	afterbody flap deflection angle, deg
$\delta_F$	wing flap deflection angle, deg
$\Lambda$	leading-edge sweep angle, deg
$\rho$	density, slugs/ft <sup>3</sup>
$\theta$	angular location of forebody pressure orifices, deg
$\phi$	rotation angle of sharp nose, deg

Configuration abbreviations:

ABF	afterbody flaps
B	body alone
C	canard (6° cone forebody configuration)

F	landing gear fairing
L	left
LS	long fuselage strake
R	right
SC	straight canard (5° cone forebody configuration)
SS	short fuselage strake
T	vertical tails
W	wing

## Model Description

Two delta wing planform accelerator-type configurations were investigated. The first configuration, referred to as the "6° cone forebody configuration," consisted of a 6° semiapex angle conical forebody with a simulated wrap-around engine package, an 8° truncated cone afterbody, a delta wing with twin vertical tails, a canard, and landing gear fairings along the sides of the forebody. This configuration was 10.74 feet long, had a wing leading-edge sweep angle of 70°, a 4-percent circular arc airfoil, and was fabricated with a fiberglass outer shell. A sketch showing the overall dimensions and the location of the model support system is presented in figure 1. The model was stung mounted on an internal, six-component, strain-gauge balance. A photograph of the model installed in the test section of the Langley 14- by 22-Foot Subsonic Tunnel is presented as figure 2.

Engine thrust was generated on the model by a simulated wrap-around engine package which contained 28 individual ejector-powered flow-through engine simulators. Each engine simulator had a high-pressure nozzle located in the rear of the inlet spike as shown in the sketch presented in figure 3. This design entrained flow into the inlet and provided exhaust flow simulation for low-speed engine operations. High-pressure air was supplied to the model through a stainless-steel air supply line. In order to minimize effects of the air line it was coiled several turns in one direction and then the same number of turns in the opposite direction. This coiled section of the air supply line was housed within the afterbody of the model as shown in figure 1. Calibration of air line pressure tares was obtained prior to model buildup and appropriate corrections were made to the balance output to minimize the effect of bridging the balance sensing elements with the air line.

Several different nose apex geometries were tested on the 6° cone forebody configuration to investigate control of forebody flow separation. These included a sharp nose, nose strakes, and an arrowhead tip, as

well as the standard nose configuration. Sketches of these nose geometries are presented in figure 4.

The second configuration tested, shown in figure 5, was similar to the 6° cone forebody configuration except for the following features: a 5° semiapex angle forebody, a larger delta wing with a diamond airfoil shape, long and short fuselage strakes, straight and delta planform canards, wing flaps deflectable  $\pm 30^\circ$  as well as afterbody flaps of a split flap design, and variable nose tip bluntness. Details of the afterbody flap positions and deflections are presented in figure 6, and the seven nose tip configurations tested are illustrated in figure 7. This second configuration is referred to as the "5° cone forebody configuration."

One final feature of the 5° cone forebody configuration was that it had numerous pressure orifices along the surface of the conical forebody. The pressure orifices were located circumferentially around the forebody at 11 longitudinal locations ranging from approximately 10 in. back from the nose to approximately 6 in. in front of the engine inlets. The orientation and exact locations of these pressure orifices are presented in figure 8.

Additional model dimensions are listed for both the configurations in table I.

## Test Conditions and Techniques

The investigations were conducted in the Langley 14- by 22-Foot Subsonic Tunnel over an angle-of-attack range from  $-4^\circ$  to  $30^\circ$  and a sideslip range from  $-20^\circ$  to  $20^\circ$ . The basic aerodynamic data were obtained at a free-stream dynamic pressure of 49 psf, which was chosen to give a thrust coefficient of 0.42 using the maximum available engine thrust of 256 lb. A thrust coefficient of 0.42 was used because it has been identified as a value representative of takeoff and approach conditions (ref. 1). Reynolds number sensitivity was investigated over the dynamic pressure range from 10 to 120 psf corresponding to a unit Reynolds number per foot from  $0.58 \times 10^6$  to  $2.02 \times 10^6$ . Flow visualization tests were conducted at  $q_\infty = 49$  psf for the water injection technique and for surface oil flows; however, because of test restrictions,  $q_\infty$  was limited to 3.5 psf for smoke flow and laser light sheet studies.

The oil flow visualization runs were conducted using a mixture of mineral oil, oleic acid, and titanium dioxide applied with a paint brush. The model attitude and test conditions were held constant while the flow pattern was established, then the tunnel was quickly brought to zero velocity and photographs were taken inside the test section. A new layer of the mineral oil mixture was then applied and the process was repeated for the next test condition.

The forces and moments on the configurations were measured with an internal strain-gauge balance capable of supporting loads of up to 3000 lb of normal force, 500 lb of axial force, 10 000 in-lb of pitching moment, 7500 in-lb of rolling moment, 4500 in-lb of yawing moment, and 1800 lb of side force. The error of these balance measurements is, at worst case,  $\pm 0.5$  percent of the maximum loadings. The pressures measured on the 5° cone forebody were obtained through an ESP (electronically scanned pressure) system capable of measuring a maximum pressure of 144 psf. The error of the pressure measurements is, at worst case,  $\pm 0.5$  psf.

## Presentation of Results

The results of the investigations are presented in the following figures:

	Figure
Longitudinal aerodynamics:	
Effects of dynamic pressure . . . . .	9
Configuration buildup . . . . .	10
Canard effects . . . . .	11
Exhaust flow visualization . . . . .	12
Power effects on positive flap deflections . . . . .	13
Power effects on positive wing flap deflections . . . . .	14
Power effects on negative flap deflections . . . . .	15
Unpowered trim analysis . . . . .	16
Effects of engine arrangement . . . . .	17
Flap effectiveness due to engine arrangement . . . . .	18
Directional characteristics:	
Effects of nose geometry . . . . .	19
Surface flow visualization with standard nose . . . . .	20
Surface flow visualization with sharp nose . . . . .	21
Surface flow visualization with canard on . . . . .	22
Off-surface flow visualization showing canard effects . . . . .	23
Effects of nose bluntness . . . . .	24
Pressure data illustrating effects of nose bluntness . . . . .	25
Effects of sharp nose rotation angle . . . . .	26
Pressure data illustrating effects of sharp nose rotation angle . . . . .	27
Configuration buildup directional stability . . . . .	28
Split flap effectiveness for yaw control . . . . .	29

## Discussion

### Longitudinal Aerodynamics

An investigation of Reynolds number effects was conducted and data are presented for axial- and normal-force coefficients as a function of free-stream dynamic pressure for the 6° cone forebody configuration in figure 9. Data are presented for the body alone as well as for the complete configuration at an angle of attack of 10°. Significant effects of Reynolds number were noted as the free-stream dynamic pressure was increased from 10 psf to approximately 40 psf. The body-alone configuration shows a marked increase in axial-force coefficient with the increase in free-stream dynamic pressure. A corresponding decrease in normal-force coefficient was also observed. These trends were eliminated when the wing was added to the configuration. Since there were no significant Reynolds number effects as  $q_\infty$  was increased above 40 psf, a free-stream dynamic pressure of 49 psf was deemed acceptable for the rest of the investigation. A broader investigation of the effects of Reynolds number on slender accelerator-type configurations was conducted at the Langley Research Center by Charles H. Fox, Jr., James M. Luckring, Harry L. Morgan, Jr., and Jarrett K. Huffman (in NASP TM-1011).

The effects of the configuration components on the longitudinal aerodynamics of the 5° cone forebody configuration are presented in figure 10. The addition of short or long fuselage strakes had almost no effect at angles of attack below 20°. At higher angles of attack there was still little effect when the short fuselage strakes were added; however, there was a slight increase in pitching moment when the long fuselage strakes were added. The addition of the straight canard produced a positive increment in pitching moment for all positive angles of attack.

The influence of the two canard planforms on the longitudinal aerodynamics is shown in figure 11. As expected, both canards provide increased nose-up pitching moment and lift. However, these data clearly show the increased lift, drag, and especially pitching moment that the delta canard configuration produced as compared with the straight canard configuration. The delta canard configuration, however, does not provide the increased lift and nose-up pitching moment relative to the straight canard configuration until angle of attack is increased above 10°. This is due to the vortex lift generated by the delta wing planform canard as well as a 37-percent greater canard area.

During the first tunnel entry, a concentrated effort was made to identify portions of the configuration flow field that would provide the best flow for control

surfaces. In particular, the afterbody flow field was explored to determine the effects of the exhaust flow from the propulsion simulators. Water was injected into the engine inlets and was entrained with the exhaust flow to provide a very effective means of exhaust flow visualization. Care was taken to ensure that the water was properly injected such that it mixed well with the inlet flow as well as the ejector flow. This flow visualization was further enhanced by the use of a laser light sheet as can be seen in the exhaust flow visualization photograph presented in figure 12. It is the significant amount of exhaust flow passing over the afterbody and the inboard portion of the wing (clearly revealed by this flow visualization technique) that led to the design and testing of inboard afterbody flaps during the second test program.

As a result of the above mentioned flow visualization, afterbody flaps were designed and positioned on the 5° cone forebody configuration such that they would be immersed in the exhaust flow as illustrated by the sketches presented in figure 6. Longitudinal aerodynamic data for various flap deflections are presented in figures 13 to 15. The power-off control effectiveness ( $\Delta C_m$ ) of the afterbody flaps remained constant with increasing angle of attack in contrast to the wing flaps, which when deflected in combination with the afterbody flaps, showed noticeable loss of effectiveness above  $\alpha = 10^\circ$  (fig. 13). The wing flaps however, even though they had losses in effectiveness at angle of attack, were more effective than the afterbody flaps. When power was added, the wing flaps provided a relatively constant level of effectiveness with angle of attack, whereas the afterbody flaps provided increased effectiveness as angle of attack was increased. When angle of attack was increased beyond 16°, a 30° afterbody flap deflection with power on produced the same amount of nose-down pitching moment as did both afterbody and wing flaps deflected 30° with power off. This illustrates the significant influence of the exhaust flow on the afterbody flaps.

Effectiveness of the wing flaps alone, with and without power, is shown in figure 14. The same trends observed for the flaps used in combination with the body flaps are evident thereby indicating that, although the two flap surfaces are relatively decoupled, they both derive substantial benefit from the power-induced afterbody flow.

In all cases involving 30° wing and/or afterbody flap deflections presented in figures 13 and 14, a nose-down pitching moment was produced across the angle-of-attack range. The moment created by the 30° flap deflections could not be countered by the



straight canard at zero incidence and a trimmed condition was not achieved.

The effects of afterbody flaps and wing flaps deflected  $-30^\circ$  (trailing edge up) are presented for both power-off and power-on conditions in figure 15. It is immediately apparent that the split flap concept used for the body flap loses much effectiveness compared with the conventional wing flap for the nose-up control function, primarily because the body flap is acting on only the upper surface flow. The benefits of power for the body flap are also substantially diminished and appear to have their largest effect on the wing flaps. This lower amount of flap effectiveness for the afterbody flaps as compared with the wing flaps was also apparent in the  $30^\circ$  flap deflection data presented in figure 13.

Even though the benefits of power-on flap effectiveness have been reduced, the  $-30^\circ$  flap deflection has provided one power-on condition that is trimmed over the approach and takeoff angle-of-attack operating range of  $10^\circ$  to  $15^\circ$ . This power-on condition, which has only afterbody flaps deflected  $-30^\circ$ , produces a lift coefficient of from 0.3 to 0.5, a drag coefficient of approximately  $-0.2$ , and essentially zero pitching moment for  $10^\circ \leq \alpha \leq 15^\circ$ , which are acceptable longitudinal aerodynamic conditions for takeoff. When approach conditions are considered, however, there was no flap setting tested that provided a trimmed condition and positive drag for  $10^\circ \leq \alpha \leq 15^\circ$ . Therefore, in order to obtain a trimmed configuration for approach conditions, additional flap deflections, power settings, and/or canard incidence angles would need to be investigated.

Longitudinal aerodynamic data for the maximum positive and negative flap deflections for both the afterbody flaps and the wing flaps are presented for the configuration with the straight canard on in figure 16. This presentation of the longitudinal data shows the available power-off pitch control and the associated available lift and drag coefficients across the angle-of-attack range tested for the configuration with the straight canard. These data indicate that this long, slender accelerator-type configuration will benefit from a high lift canard, as this will allow reduced trailing-edge-up flap deflections to trim the configuration. Trailing-edge-up flap deflections are not desirable during low-speed operations due to the resulting reduction in overall configuration lift.

An alternate engine configuration was tested in which all the engines on the top of the configuration were removed and then replaced with a smooth faired surface. Both power-off and power-on longitudinal aerodynamic data are presented for all engines on as well as for engines on only the bottom half of the fuselage in figure 17. Even though exactly one half

the engines were removed and the supply air pressure was unchanged, the power-on  $C_T$  was greater than one half the power-on  $C_T$  for the configuration with all engines on. This was due to a more efficient performance of the lower surface engines. Two differences between these two engine configurations are noted when comparing the longitudinal data for power-on conditions. First, the configuration with all engines on produces an increase in  $C_L$  for  $\alpha \geq 8^\circ$  due to exhaust flow over the wing, whereas the configuration with engines only on the lower half of the fuselage produces essentially no additional lift. Second, the configuration with all engines on produces a slight increment in nose-down pitching moment for angles of attack greater than  $10^\circ$ . In contrast, the configuration with bottom engines only produces a nose-up increment in pitching moment across the entire angle-of-attack range. This nose-up moment would be expected due to the thrust vector acting below the moment reference center of the model. This inherent nose-up moment for the powered configuration with bottom engines only acts to improve pitching-moment characteristics as illustrated by the trimmed condition at  $\alpha = 12^\circ$  for the undeflected flap condition.

Longitudinal aerodynamic data showing the effects of the exhaust flow on  $30^\circ$  flap deflections for both engine configurations are presented in figure 18. As expected, there was a greater increase in flap effectiveness during power-on conditions for the configuration with all engines than there was for the configuration with bottom engines only. This was due to the exhaust flow adding energy to the flow over the flaps on both the upper and lower surfaces on the configuration with all engines, whereas only the lower surface flow was energized on the configuration with bottom engines only. When the two engine configurations are compared during power-off conditions, the configuration with bottom engines only generates more lift and has slightly better flap effectiveness. This is due to the absence of engines on the upper half of the fuselage and thus smoother, undisrupted flow over the inboard afterbody flaps.

### Directional Characteristics

Investigation of the directional aerodynamics focused on determining potential levels of side force and yawing moment at zero sideslip due to an asymmetric forebody flow field. It is important to determine if such out-of-trim moments and side forces might occur at angles of attack within the expected operational flight envelope of such advanced vehicles. The ability to trim such asymmetries in approach and landing must be provided by the lateral/directional control devices.

In particular, the  $6^\circ$  cone forebody model was used initially to explore the basic forebody characteristics and the influence of major configuration features such as nose strakes and canards. Additional low-speed tests on these configuration concepts were conducted in the Langley 14- by 22-Foot Subsonic Tunnel by John W. Paulson, Jr., P. Frank Quinto, Daniel W. Banks, and Gregory M. Gatlin (in NASP TM-1012). A more refined effort was undertaken using the  $5^\circ$  cone forebody model to systematically address nose bluntness and to determine the surface pressure loadings produced by the strong vortical flows. The maximum angle of attack tested was limited for several configurations due to severe model/sting oscillations arising from the nose flow asymmetries.

**$6^\circ$  cone forebody model.** A series of different forebody apex geometries, as illustrated in figure 4, were explored on the  $6^\circ$  cone forebody model, and the measured directional aerodynamics are shown in figure 19. Results show the expected side force at the higher angles of attack for the sharp nose configuration. This is due to the unstable asymmetric vortical flows above the forebody. Experience has shown that minute model imperfections will influence the sense of the asymmetry (ref. 3). Similarly, small asymmetries in geometry, as would occur for the various nose changes, would be expected to cause the sense of the flow asymmetry, and thus the side force, to change as illustrated in the data of figure 19. The nose strake configurations tested were likely to introduce slight geometric asymmetries and thus were ineffective in suppressing the asymmetric forebody flow field. When the canard configuration was tested, however, there was minimal side force and yawing moment as angle of attack was increased beyond  $16^\circ$  when compared with the other configurations. The canard appeared to weaken or move the vortices from the nose such that no strong asymmetric loadings could be established.

In order to investigate the characteristics of the forebody flow field more thoroughly, both on- and off-surface flow visualization studies were conducted. The surface flow characteristics of the model were displayed with oil flow patterns as illustrated in figures 20 to 22. The  $6^\circ$  cone forebody configuration with the standard nose is presented at  $16^\circ$  angle of attack in figure 20. This angle of attack is below the onset of the large side forces and displays relatively symmetric vortical flow as noted by the flow pattern over the leeward side of the forebody. In addition, these surface flow visualization photographs indicate substantial inlet flow disturbances. The vortex sep-

aration and reattachment lines in figure 20(a) reveal that the leeward-side vortices were ingested by the upper engine inlets. The side-view photograph in figure 20(b) shows that the flow sweeping around the forebody at angle of attack enters the inlet at substantial angles, noticeably misaligned with the inlet sidewalls. The position of the landing gear fairing, however, tends to reduce the degree of misalignment.

The flow visualization photograph presented in figure 21 shows surface flow patterns for the sharp nose configuration at  $\alpha = 18^\circ$  and  $\beta = 0^\circ$ . Here the asymmetric flow pattern is clearly evident as the forebody vortices have shifted toward the right side of the model. The right-hand secondary vortex separation line was not present; this indicates that the vortex sheet had "peeled off" the body. This flow pattern is associated with the asymmetric side force which is responsible for the yawing moments observed.

Surface oil flow visualization is presented for the standard nose configuration with the canard on in figure 22. This configuration can be compared directly with figure 20(a) (canard off) to identify the effects of the canard on the forebody flow field. It is evident that the canard either disrupted or repositioned the vortices from the nose so that the strong vortex flow influence on the forebody was no longer present. This result correlates with the small absolute values of  $C_n$  and  $C_Y$  presented for the canard configuration in figure 19.

A visualization of the off-surface vortex flow to assess the canard influence is presented in figure 23. The flow visualization was conducted at a free-stream dynamic pressure of 3.4 psf by injecting smoke upstream of the model and then illuminating the vortical flow pattern with a laser light sheet positioned perpendicular to the free stream. These photographs illustrate how the vortices from the nose stay close to the upper surface of the forebody when the canard is off and how the canard-on configuration tends to lift the vortical flow up off the surface of the forebody. This is in agreement with the surface oil flow visualization photographs presented previously.

**$5^\circ$  cone forebody model.** Tests conducted with the  $5^\circ$  cone forebody model provided a systematic look at nose bluntness and forebody surface pressure loadings to better understand the observed large flow asymmetries.

The  $5^\circ$  cone forebody model was designed to test seven variations of nose tip bluntness as illustrated in figure 7. Both yawing-moment and side-force coefficient data are presented for each of these nose tip configurations in figure 24. These data illustrate that only modest increases in nose bluntness can

produce substantial reductions in the asymmetric forces and moments, thereby providing a powerful configuration design parameter.

A more detailed description of the effects of increasing the nose tip bluntness was obtained through surface pressure measurements on the forebody. Surface pressures were obtained circumferentially around the forebody at 11 longitudinal locations as identified in figure 8, and these data are presented in pressure coefficient form for four of the nose tip configurations in figure 25. These pressure coefficient data are presented at an angle of attack of  $24^\circ$  and reveal the asymmetric flow patterns implied in figure 24. The asymmetric  $C_p$  profile evident for the sharp nose configuration stands in contrast to the more symmetric patterns obtained with increased nose bluntness, which correlates well with the oil flow patterns shown in figures 20 and 21. A final point of interest in the pressure data is that the strong asymmetric upper surface vortex flow on the sharp nose configuration switches from the right side of the forebody ( $0^\circ < \theta < 180^\circ$ ) to the left side of the forebody ( $180^\circ < \theta < 360^\circ$ ) as it moves downstream. The probable alternating local side force produced by such a pressure distribution has been observed in past forebody aerodynamic tests.

To further establish the sensitivity of the forebody flow field to small nonuniformities of the sharp nose configuration, tests were conducted in which the sharp nose was rotated in  $45^\circ$  increments and both directional data and forebody surface pressure data were obtained at each rotation angle. The directional data for these sharp nose rotation angles are presented in figure 26. Both  $C_n$  and  $C_Y$  clearly illustrate that the rotation angle of the sharp nose can have a major effect on the sense of the asymmetric forebody flow field. Forebody surface pressure data are presented at an angle of attack of  $24^\circ$  for the sharp nose configuration at rotation angles of  $90^\circ$  in figure 27. An asymmetric flow pattern is evident at each of the pressure instrumented stations along the fuselage. These surface pressure asymmetries correlate well with the asymmetric directional data presented in figure 26. Thus, when relatively small nose radii are used on such slender designs, extremely small asymmetries in the tip geometry can determine the sense of the asymmetric flow field.

The effects of various components of the  $6^\circ$  cone forebody configuration on directional stability at  $\alpha = 8^\circ$  are presented in figure 28. These data show that the configuration is directionally unstable without the twin vertical tails and that it is just slightly directionally stable with the twin vertical tails. A

value of  $C_{n\beta} = 0.002$  per degree would be a reasonable level for a configuration of this type and was obtained on a similar configuration with approximately three times greater vertical tail area as noted in reference 1. The data of figure 28 show that the complete configuration produces a value of  $C_{n\beta}$  of only approximately 0.0001 per degree. Therefore, increased directional stability would be required and thus could be achieved by increasing the area of the twin vertical tails.

In view of the substantial yawing-moment asymmetries noted earlier, the effectiveness of an asymmetric afterbody flap deflection for yaw control was investigated for both unpowered and powered conditions on both engine configurations. The afterbody flap was deflected in a split flap manner, as illustrated in figure 6(a), and data for both  $C_n$  and  $C_Y$  are presented versus angle of attack in figure 29. These data were obtained from tests on the  $5^\circ$  cone forebody configuration which had no vertical tails; therefore no direct comparisons with rudder effectiveness could be made. Data were obtained, however, from reference 1 for a similar configuration and are presented in figure 29 to indicate the yawing moment available for a  $-30^\circ$  rudder deflection on twin vertical tails. Power-off control data show neither rudders nor split flaps can provide the 0.04 level of  $C_n$  needed to offset the asymmetries noted earlier in figure 24. However, as power is added, the split flap concept (for both engine configurations) approaches the level of effectiveness needed. In addition, it should be noted that as angle of attack is increased there is, in general, a slight increase in yawing moment for the asymmetric split flap configurations. In contrast, however, there is a loss in the effectiveness of the rudders for yaw control as angle of attack is increased. These results further emphasize the potential need for powered controls on such slender aircraft designs where available controls are small in size and act on small moment arms.

## Summary of Results

The results of investigations of two delta wing accelerator-type configurations tested in the Langley 14- by 22-Foot Subsonic Tunnel are summarized as follows:

1. These slender cone-body configurations exhibited large side forces at zero sideslip at angles of attack above  $16^\circ$  due to asymmetric forebody vortex flow.
2. Small increases in nose bluntness on the forebody or the use of a canard resulted in large reductions in side forces. Changes in the roll orientation of a sharp nose tip showed substantial but consistent effects on the zero-sideslip side forces.

3. Control effectiveness obtained from aft-mounted conventional and split flaps was dramatically enhanced by the propulsion simulation exhaust flow.
4. Flow visualization showed that strong vortical flows shed from the forebody leeward side at moderate angles of attack appear to pass into the engine inlets creating the potential for substantial inlet flow disturbances.

NASA Langley Research Center  
Hampton, VA 23665-5225  
September 11, 1989

## References

1. Hahne, David E.; Riebe, Gregory D.; Riley, Donald R.; and Pegg, Robert J.: *Exploratory Wind-Tunnel Investigation of the Low-Speed Aerodynamic Characteristics of a Conical Aerospace Plane Concept*. NASA TP-2860, 1989.
2. Keener, E. R.; and Chapman, G. T.: *Onset of Aerodynamic Side Forces at Zero Sideslip in Symmetric Forebodies at High Angles of Attack*. AIAA Paper 74-770, Aug. 1974.
3. Keener, Earl R.: *Flow-Separation Patterns on Symmetric Forebodies*. NASA TM-86016, 1986.

Table I. Basic Model Geometry

(a) 6° Cone Forebody Configuration

Overall length, in.	128.88
Forebody length, in.	88.48
Wing:	
$b$ , in.	50.52
$\bar{c}$ , in.	34.89
$S$ (theoretical), in <sup>2</sup>	1750.61
$\Lambda$ , deg	70
Canard:	
$b$ , in.	20.80
$\bar{c}$ , in.	3.37
$S$ (exposed), in <sup>2</sup>	57.90
$\Lambda$ , deg	16
Vertical tails:	
$b$ , in.	6.40
$\bar{c}$ , in.	5.18
$S$ (theoretical, one side), in <sup>2</sup>	31.24
$\Lambda$ , deg	72

(b) 5° Cone Forebody Configuration

Overall length, in.	142.60
Forebody length, in.	106.29
Wing:	
$b$ , in.	43.30
$\bar{c}$ , in.	57.73
$S$ (theoretical), in <sup>2</sup>	1874.88
$\Lambda$ , deg	76
Straight canard:	
$b$ , in.	24.00
$\bar{c}$ , in.	4.11
$S$ (exposed), in <sup>2</sup>	78.66
$\Lambda$ , deg	16
Delta canard:	
$b$ , in.	19.62
$\bar{c}$ , in.	7.95
$S$ (exposed), in <sup>2</sup>	108.02
$\Lambda$ , deg	65

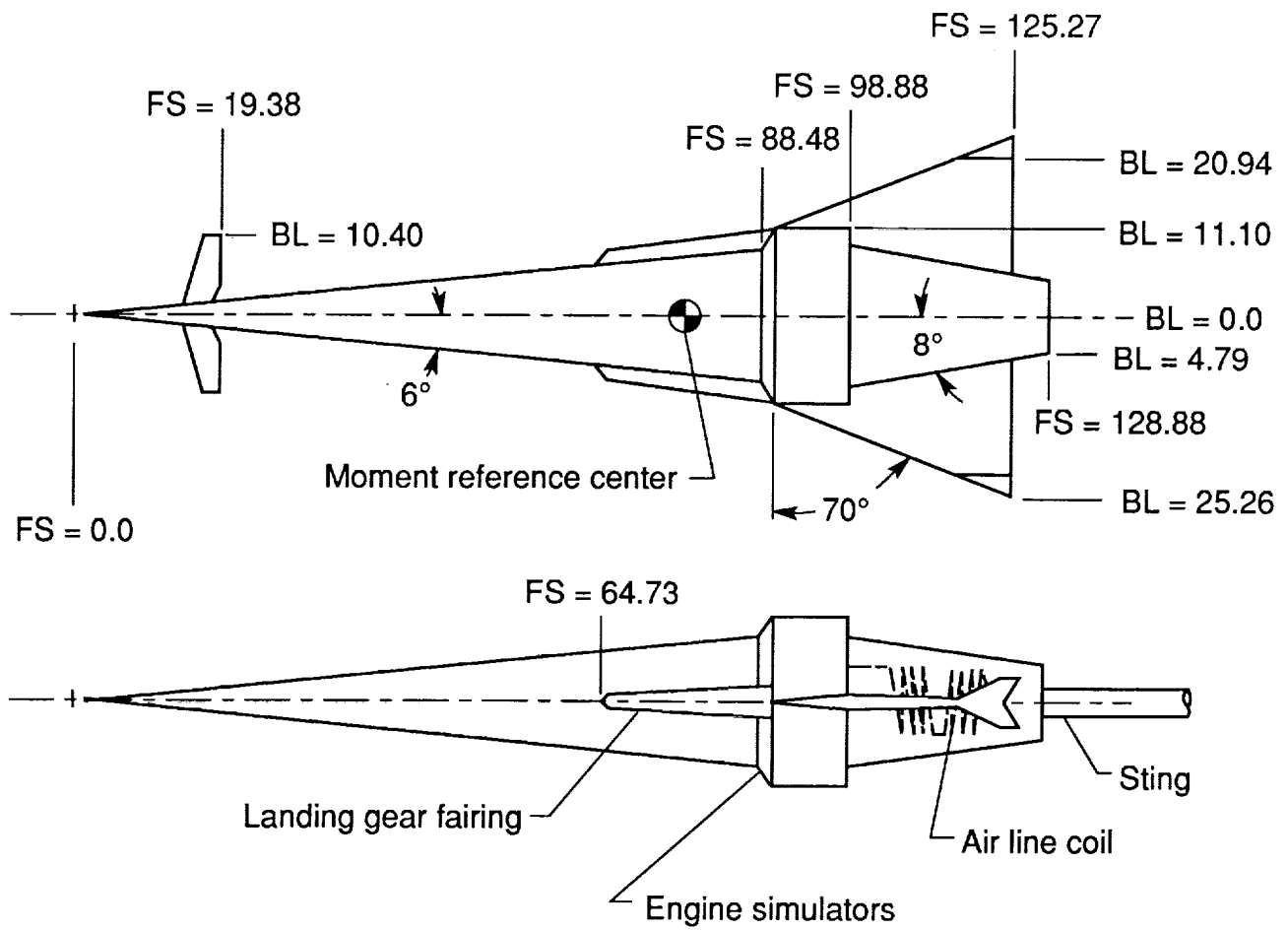


Figure 1. Geometry sketches of 6° cone forebody accelerator-type configuration. All dimensions are in inches unless otherwise noted.



L-88-1537

Figure 2. Installation of 6° cone forebody configuration in Langley 14- by 22-Foot Subsonic Tunnel.

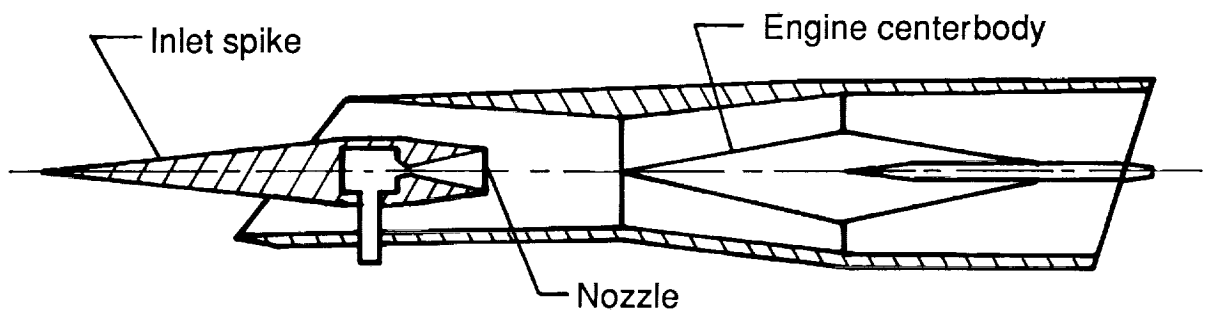


Figure 3. Cross-sectional view of one engine simulator.

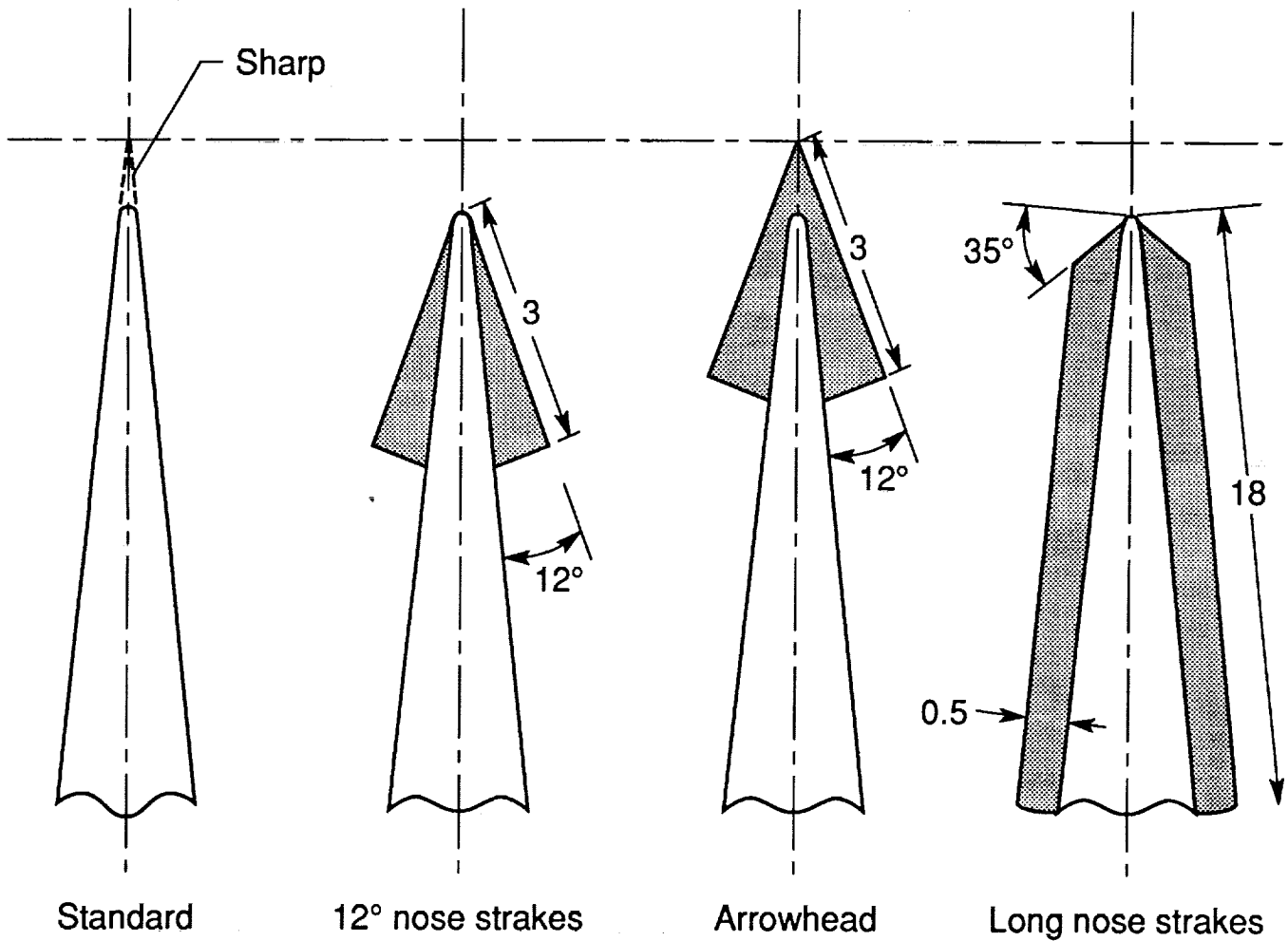


Figure 4. Nose apex planforms investigated on 6° cone forebody configuration. Linear dimensions are in inches.



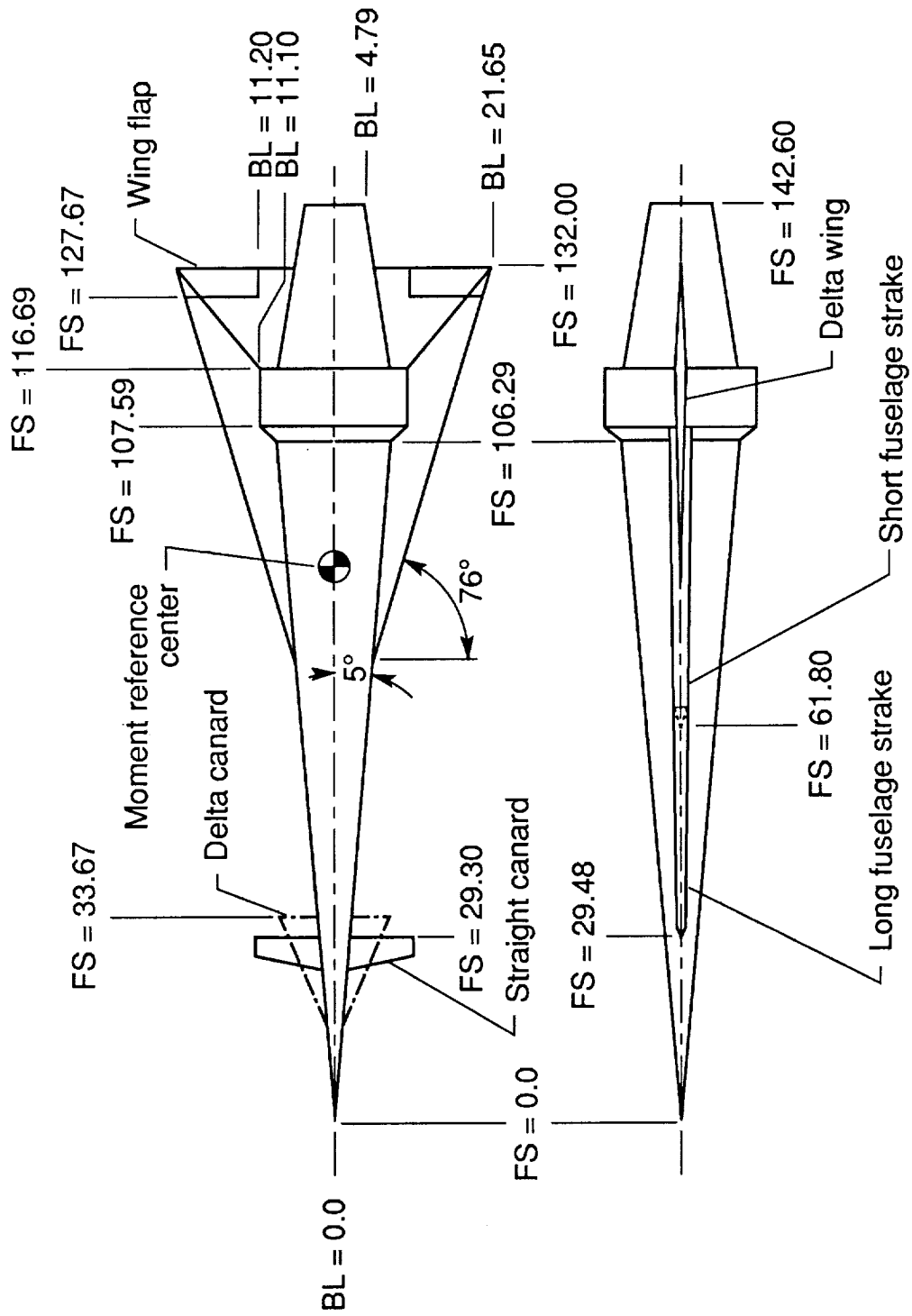
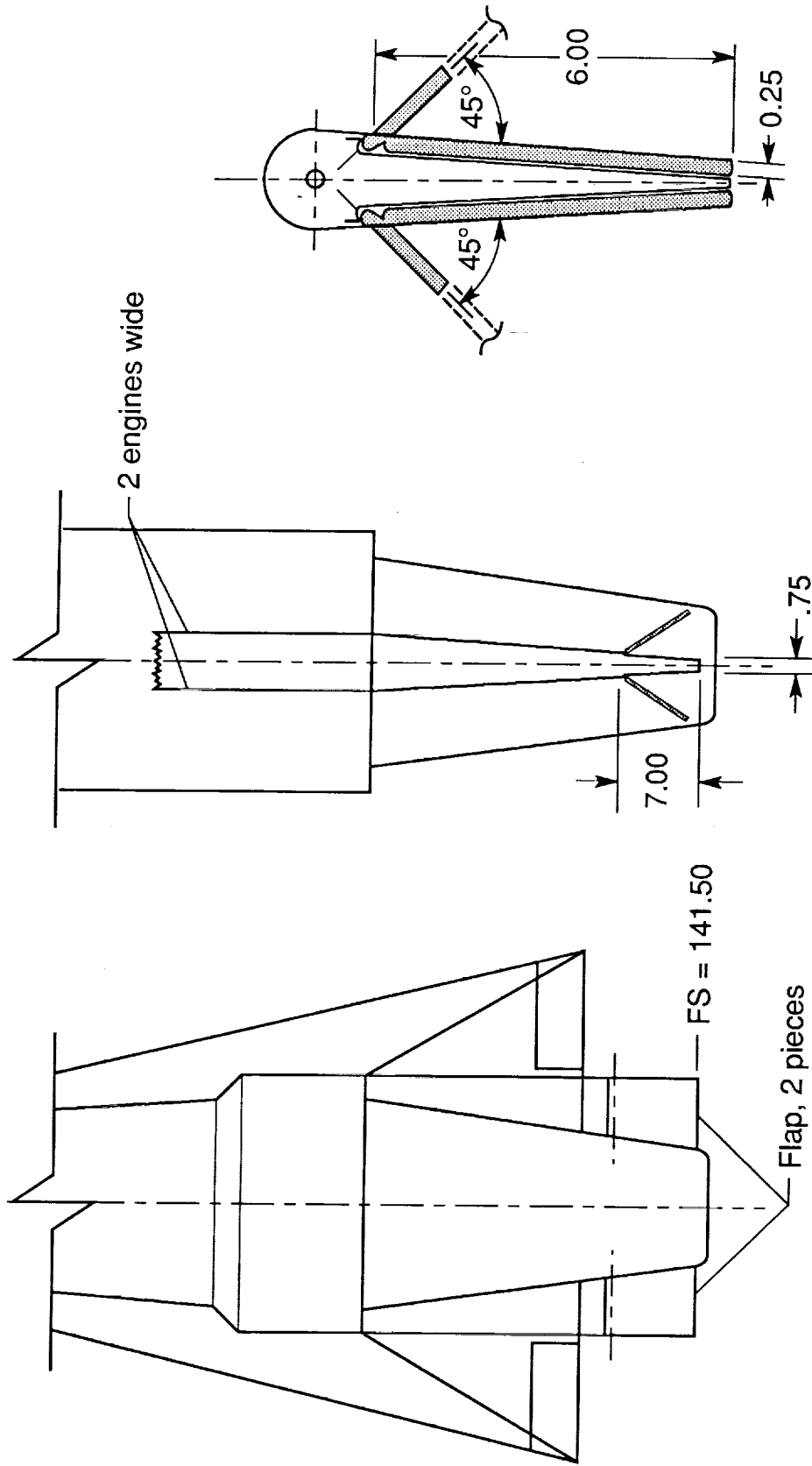
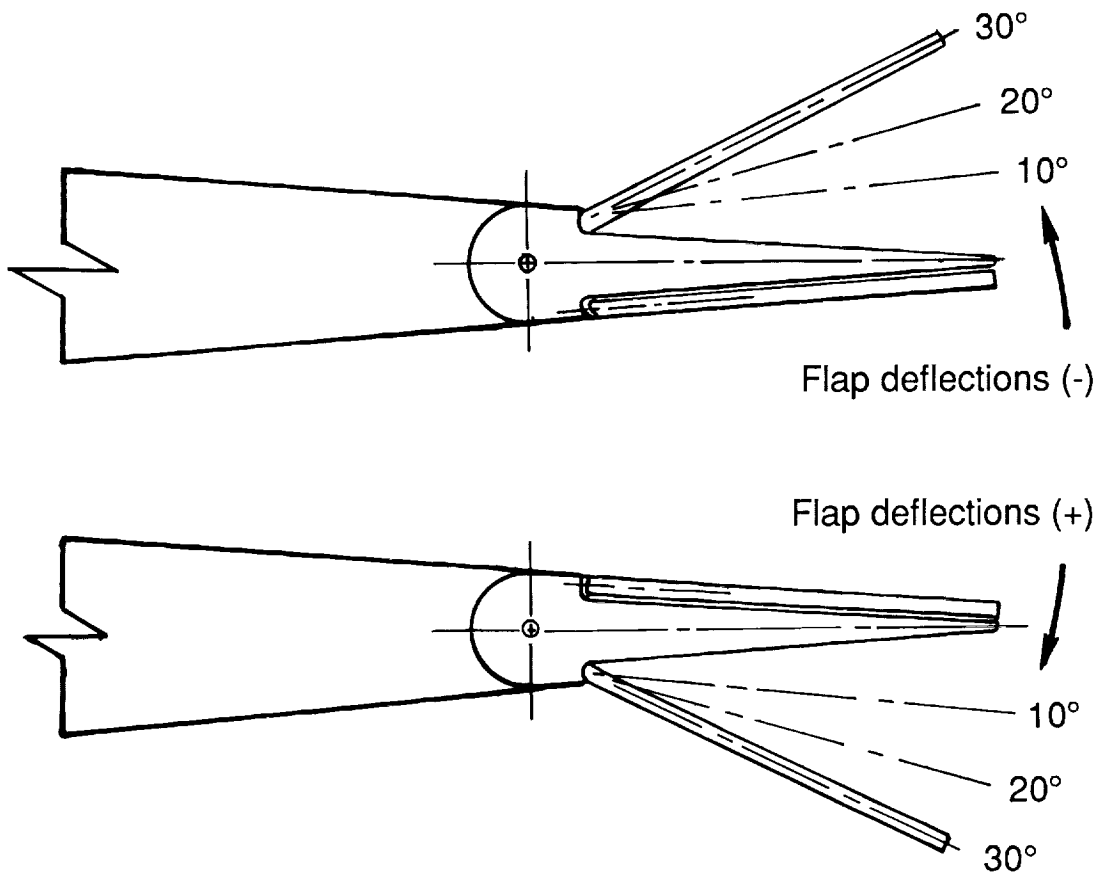


Figure 5. Geometry sketches of 5° cone forebody configuration. All dimensions are in inches unless otherwise noted.



(a) Illustrations of 45° split flap deflection for yaw control.

Figure 6. Details of afterbody flaps on 5° cone forebody configuration. All dimensions are in inches unless otherwise noted.



(b) Illustrations of positive and negative afterbody flap deflections for pitch control.

Figure 6. Concluded.

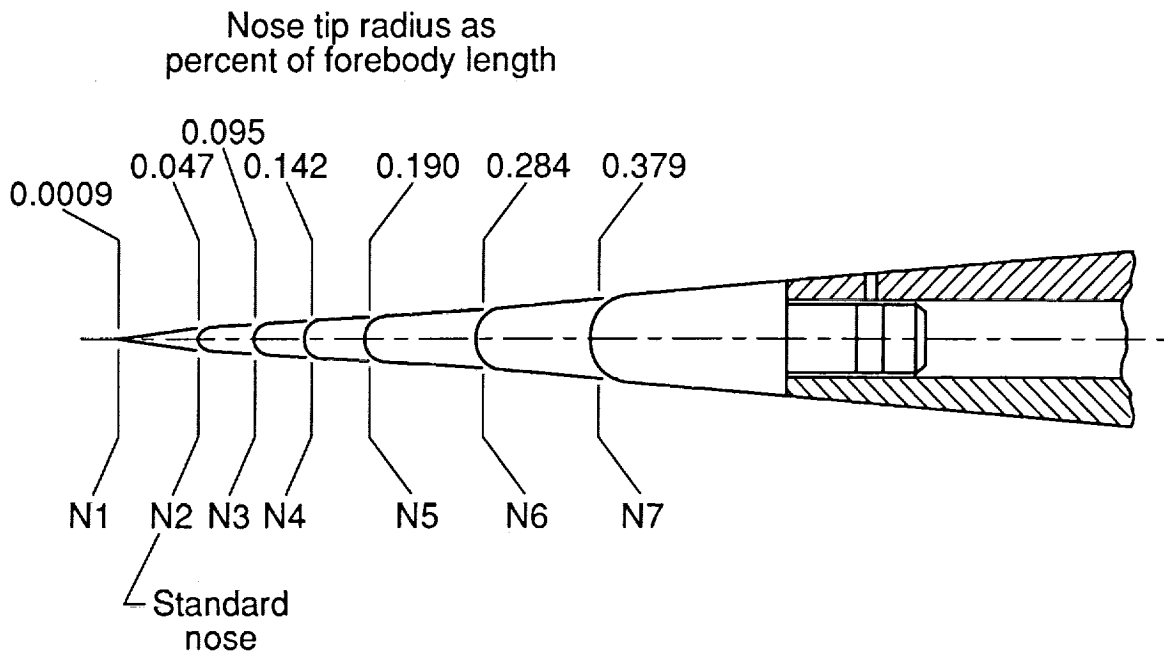
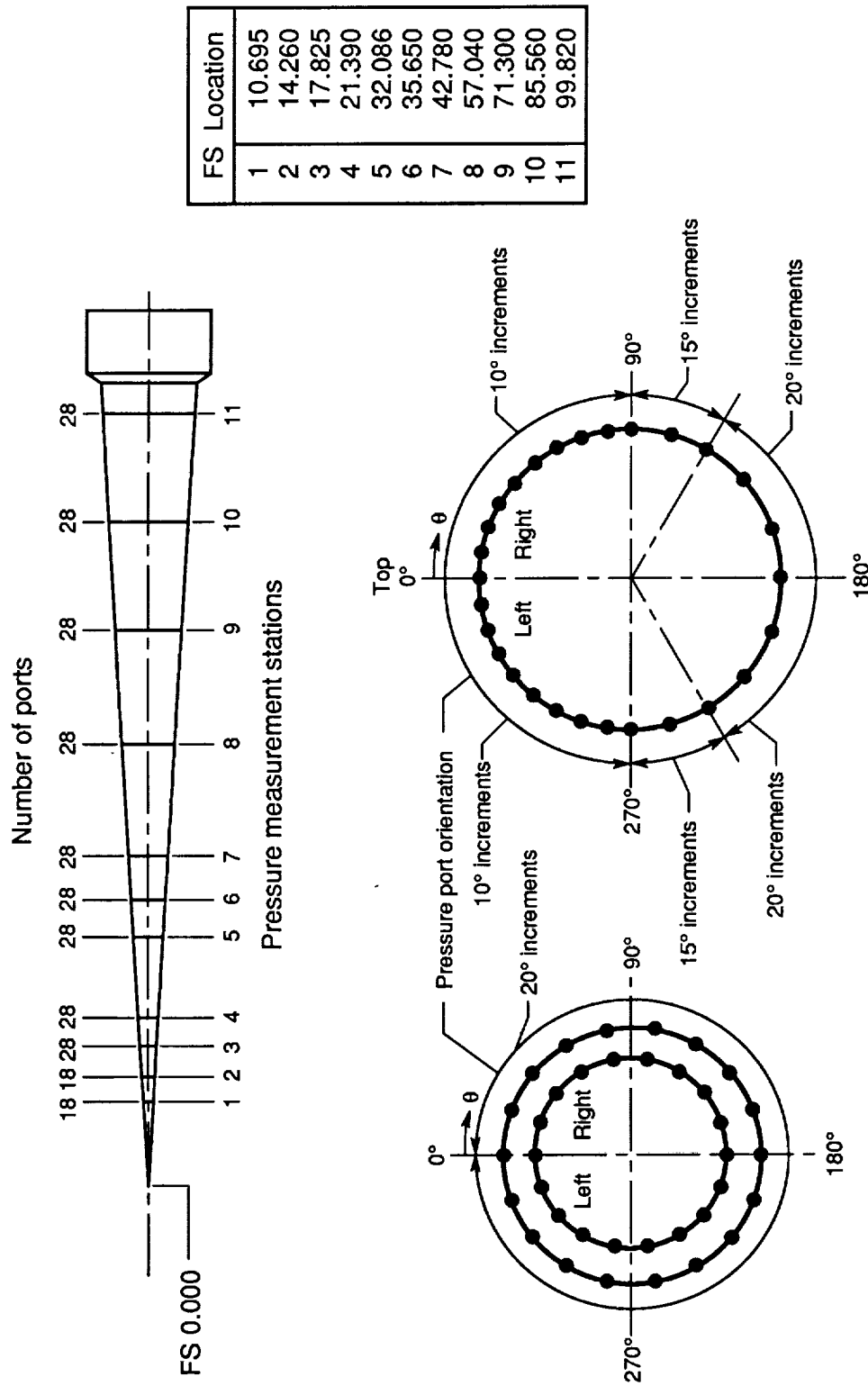


Figure 7. Nose tip bluntness configurations investigated on  $5^\circ$  cone forebody configuration. All dimensions are in inches.



18 ports each for FS 10.695 & 14.260      28 ports each for FS 17.825 through 99.820

Figure 8. Details of location of forebody pressure orifices on 5° cone forebody configuration. Pressure instrumentation = 288 ports total.

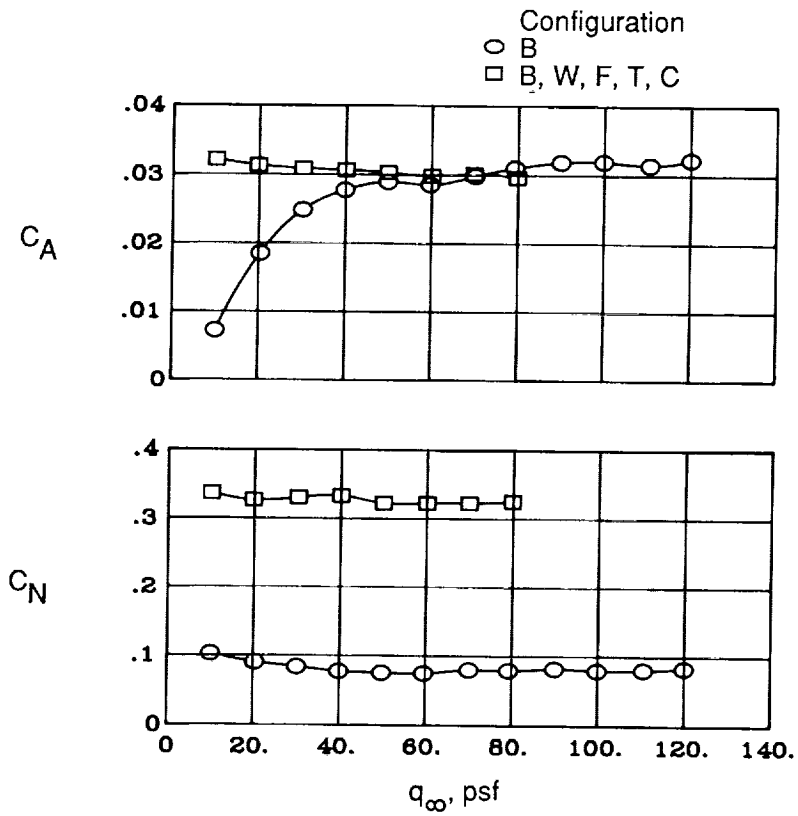


Figure 9. Effect of dynamic pressure on axial- and normal-force coefficients.  $6^\circ$  cone forebody;  $\alpha = 10^\circ$ ;  $C_T = 0$ .

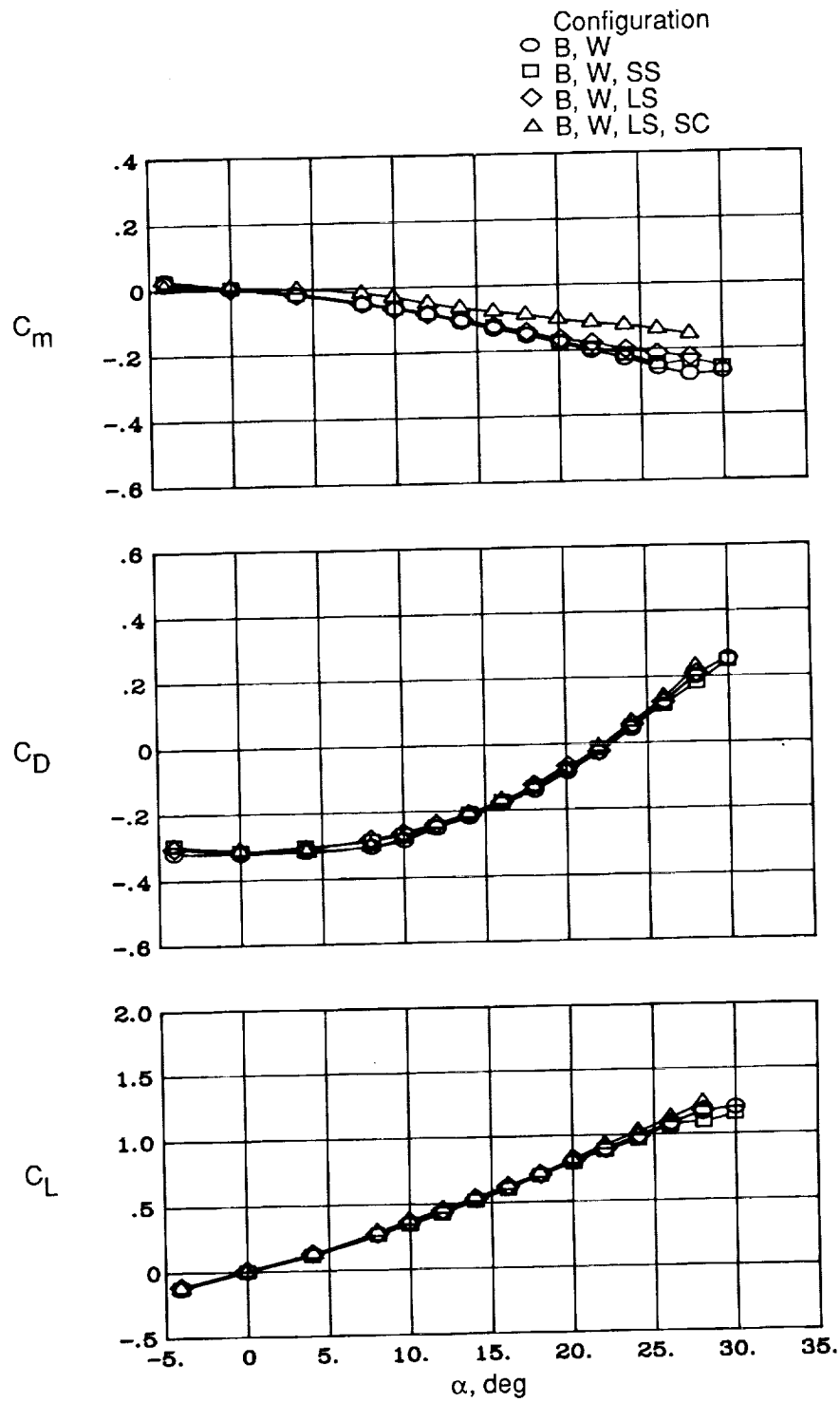


Figure 10. Longitudinal aerodynamics for configuration buildup.  $5^\circ$  cone afterbody;  $C_T = 0.42$ .

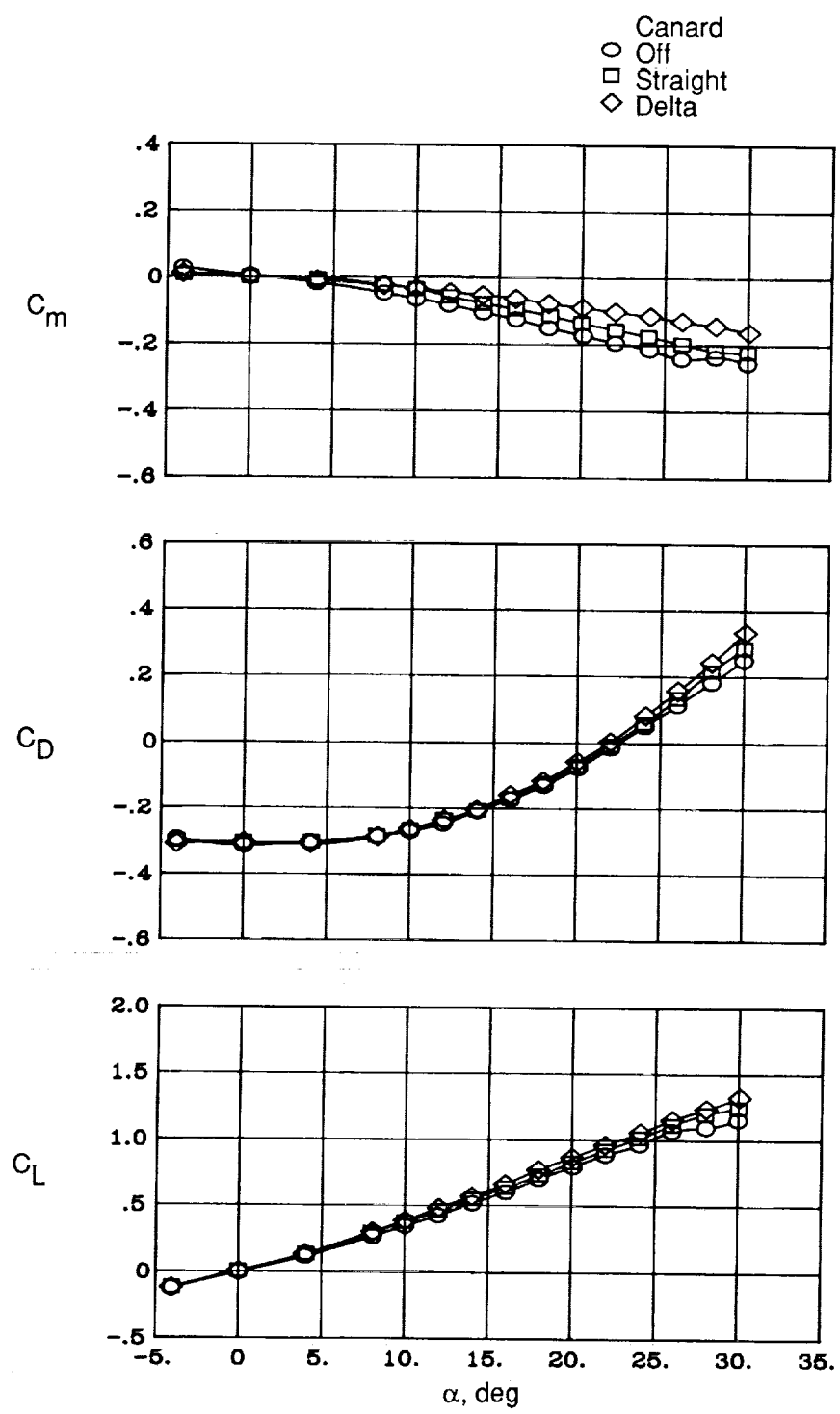


Figure 11. Effects of straight wing planform canard versus delta wing planform canard on longitudinal aerodynamics.  $5^\circ$  cone forebody; B, W, SS;  $C_T = 0.42$ .





L-89-05657

Figure 12. Exhaust flow visualization using water injection and laser light sheet.  $6^\circ$  cone forebody; B, W, F, T, C;  $\alpha = 12^\circ$ ;  $C_T = 0.42$

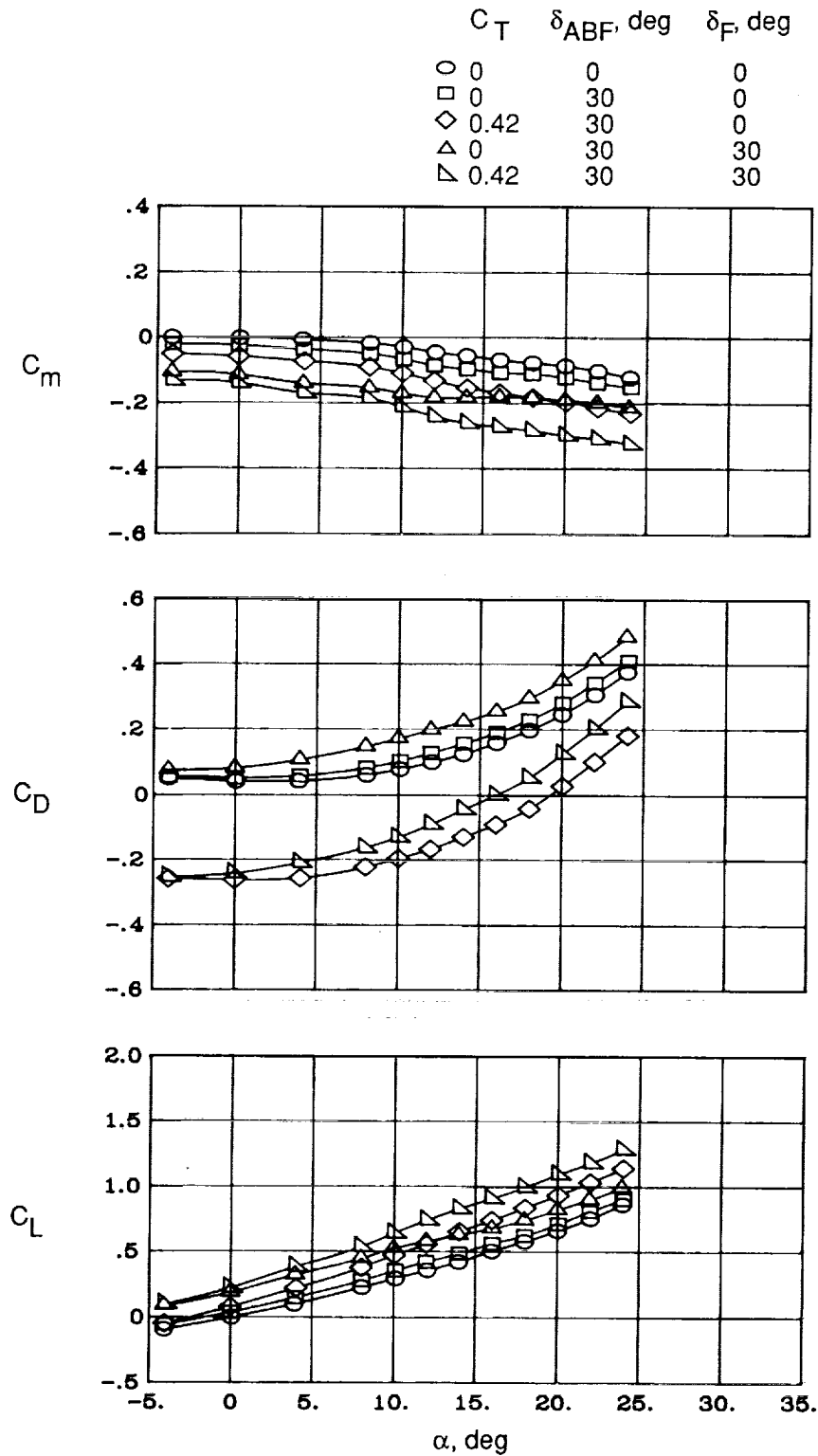


Figure 13. Effects of power on positive flap deflections. 5° cone forebody; B, W, LS, SC, ABF.

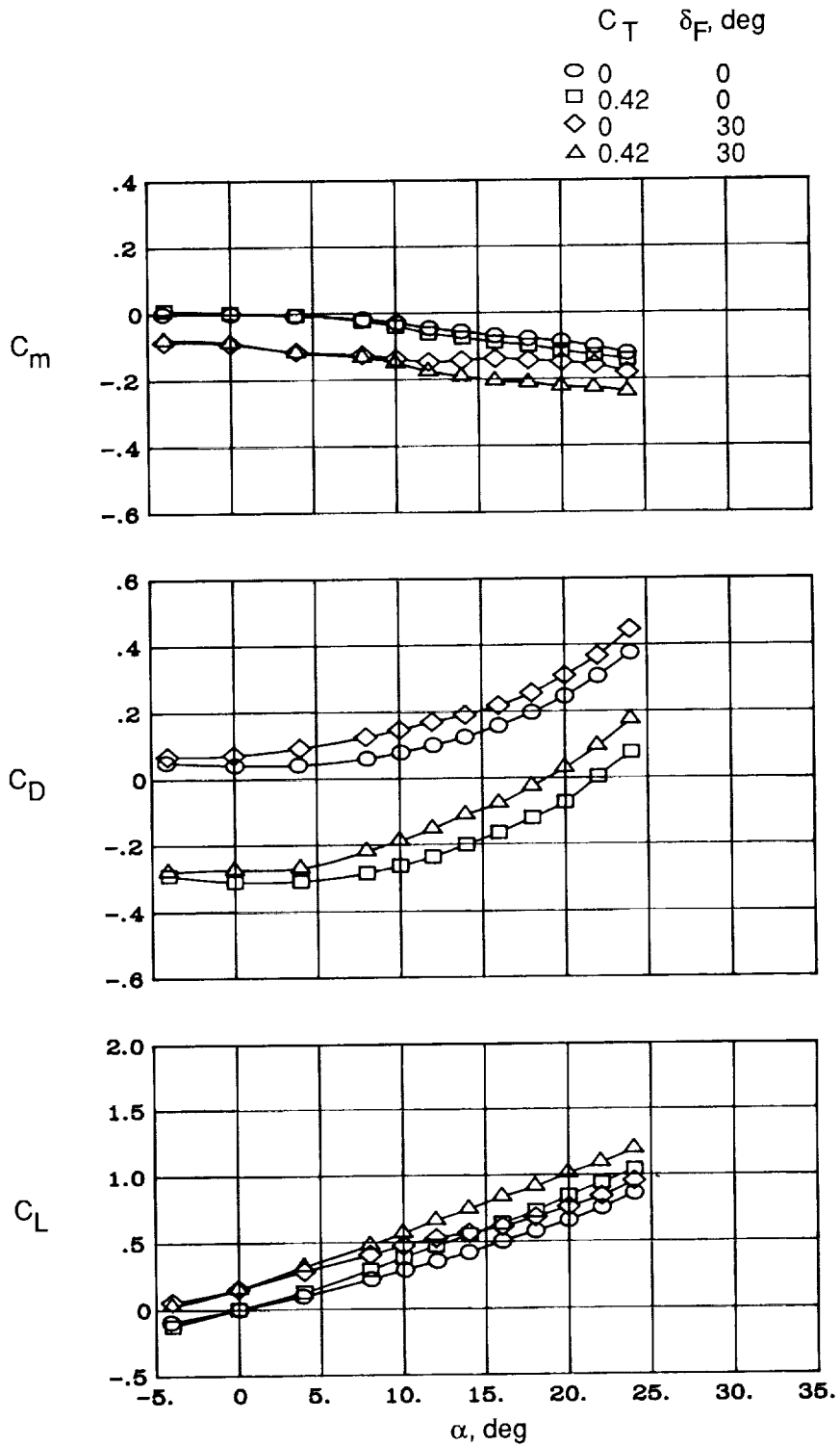


Figure 14. Effects of power on positive wing flap deflections.  $5^\circ$  cone forebody; B, W, LS, SC, ABF;  $\delta_{ABF} = 0^\circ$ .

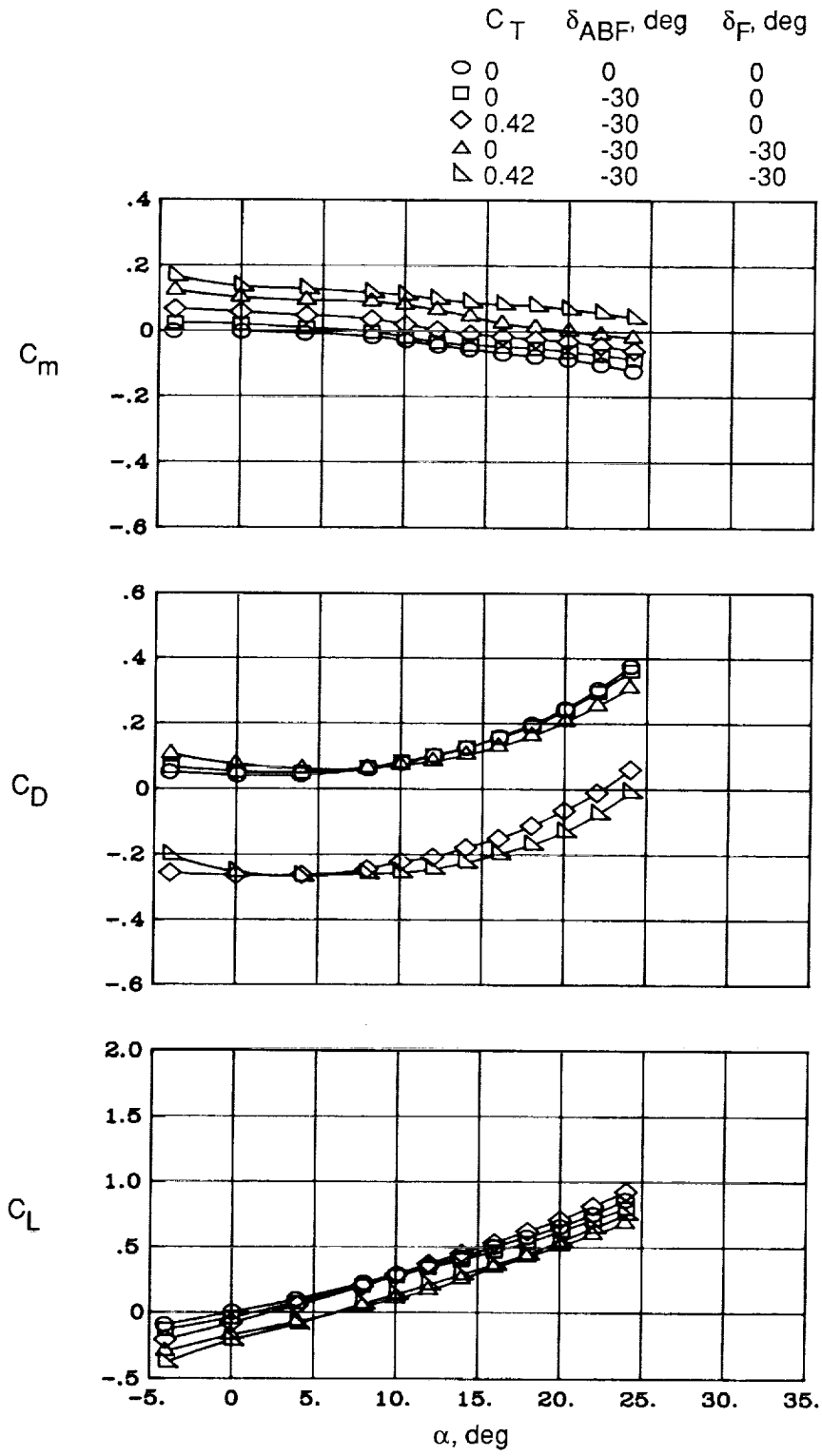


Figure 15. Effects of power on negative flap deflections.  $5^\circ$  cone forebody; B, W, LS, SC, ABF.

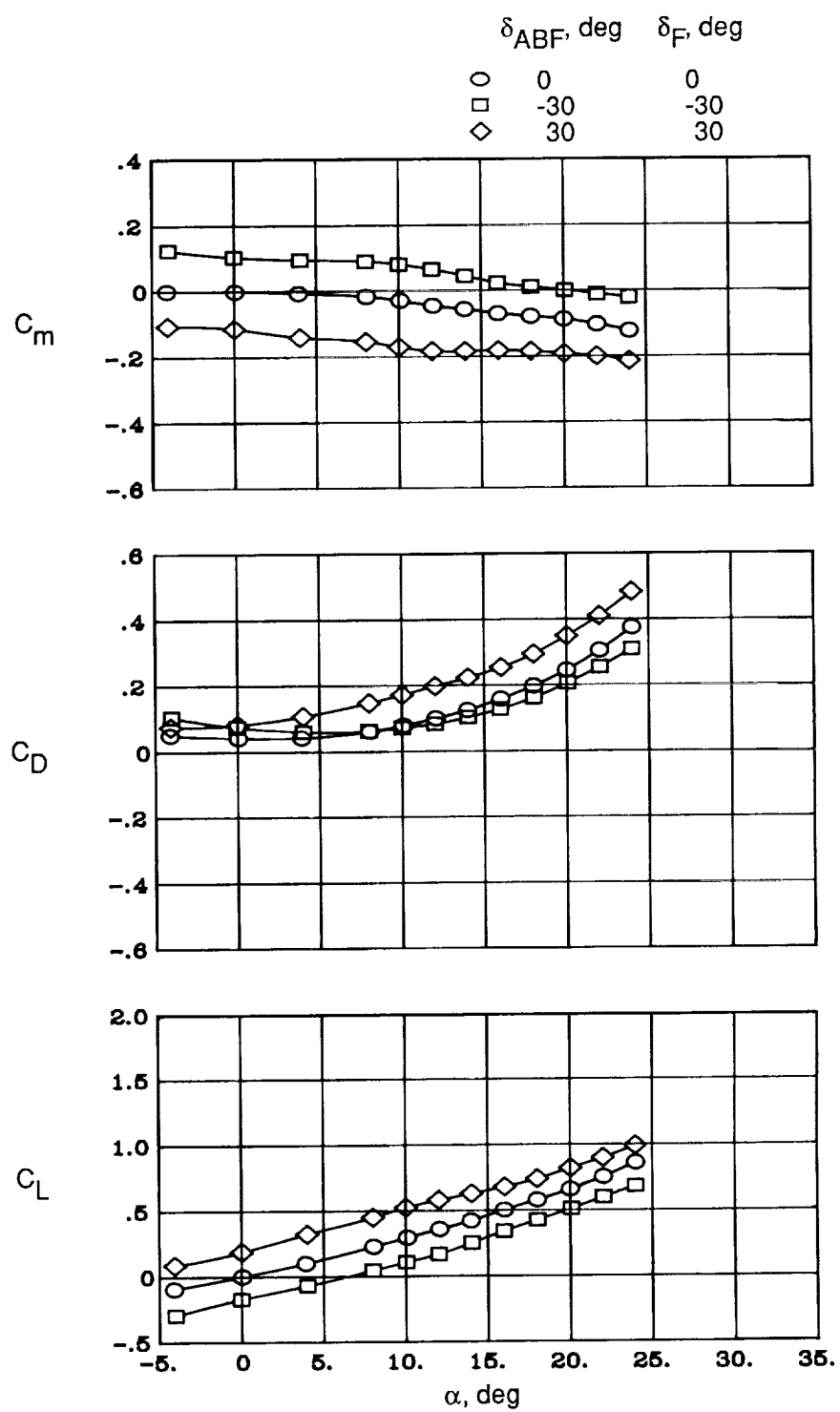


Figure 16. Unpowered trim analysis with straight canard on.  $5^\circ$  cone forebody; B, W, LS, SC, ABF.

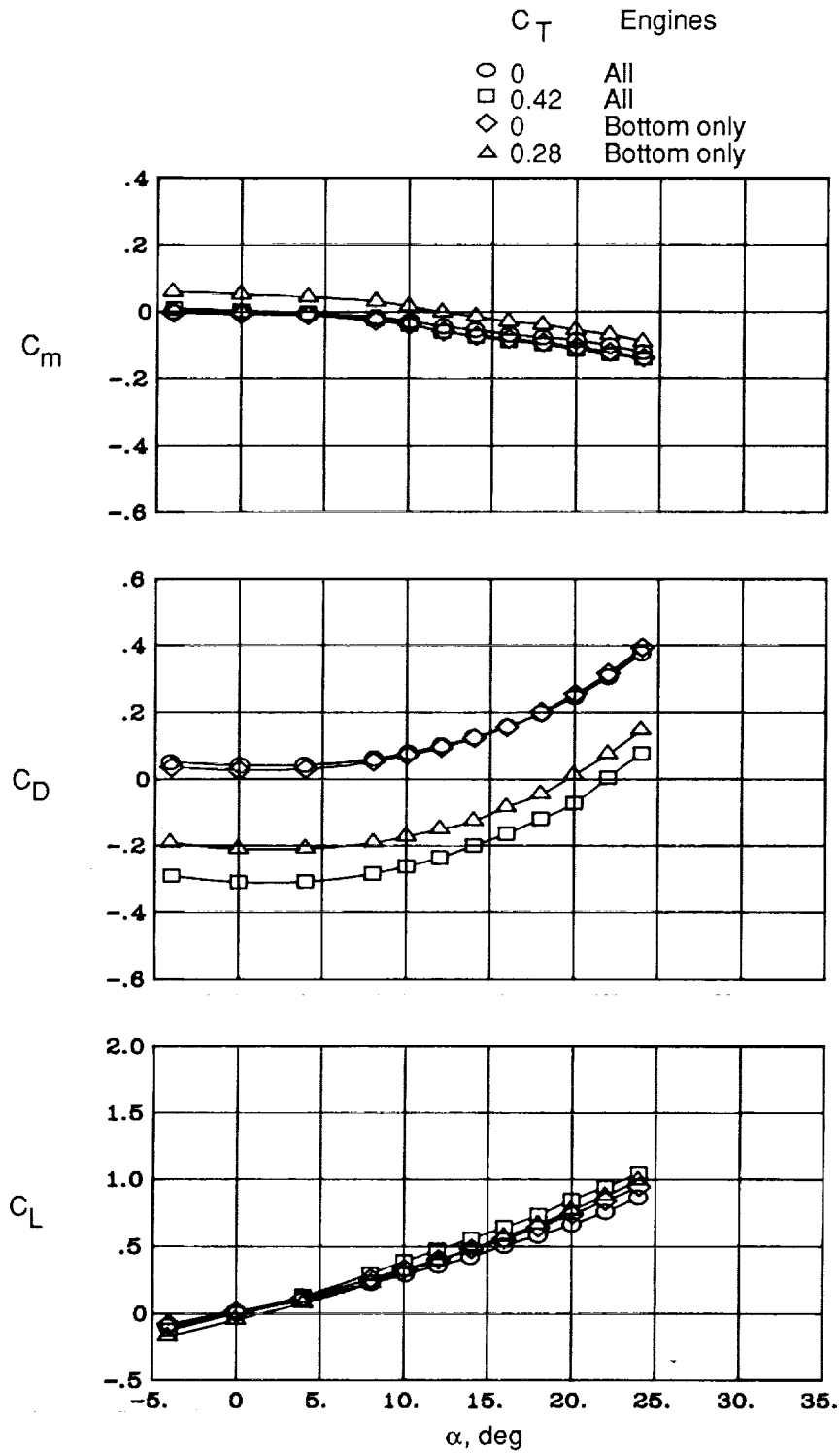


Figure 17. Effects of all engines versus bottom engines only on longitudinal aerodynamics.  $5^\circ$  cone forebody; B, W, LS, SC, ABF.

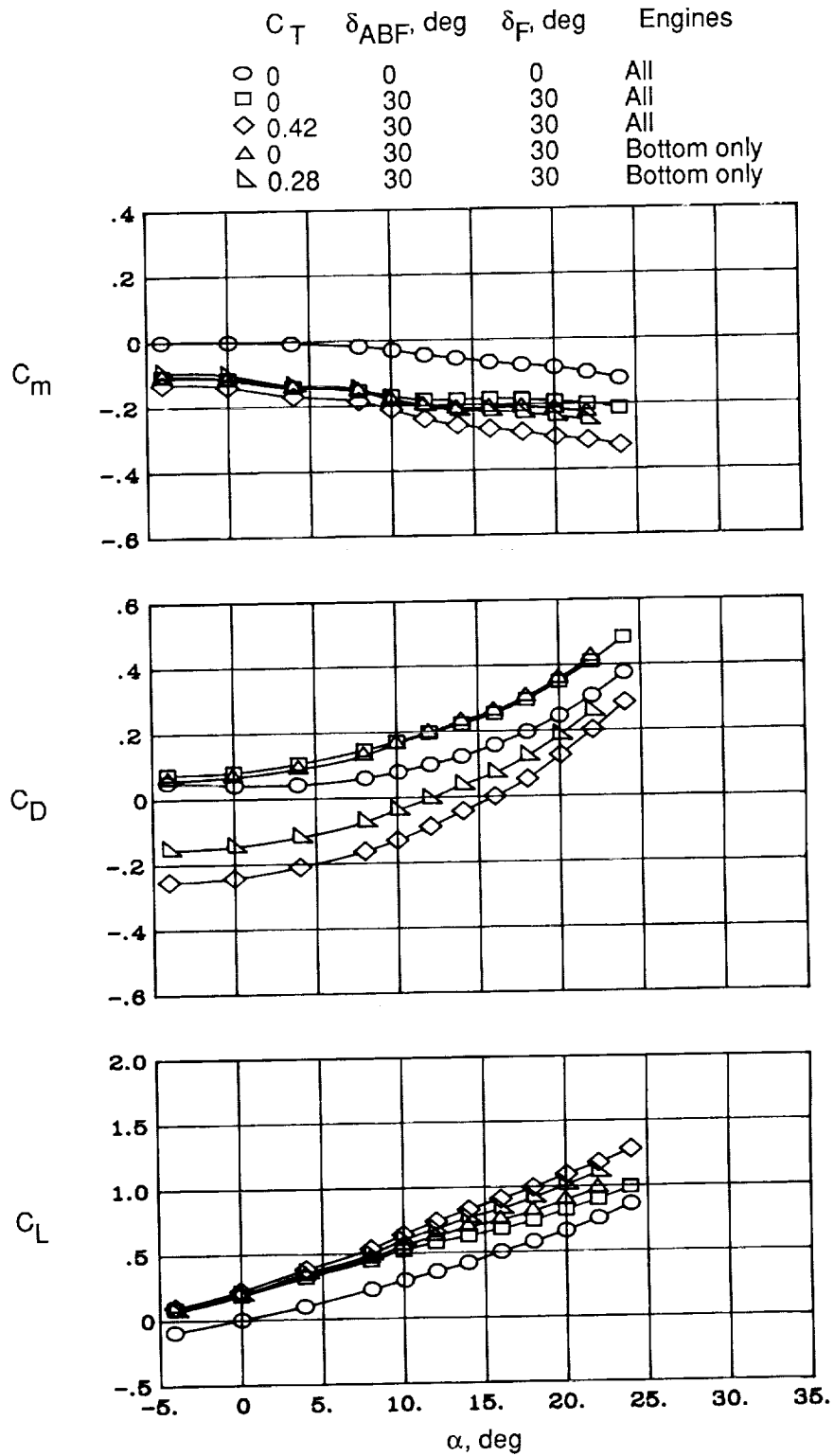


Figure 18. Flap effectiveness for all engines and bottom engines only.  $5^\circ$  cone forebody; B, W, LS, SC, ABF.

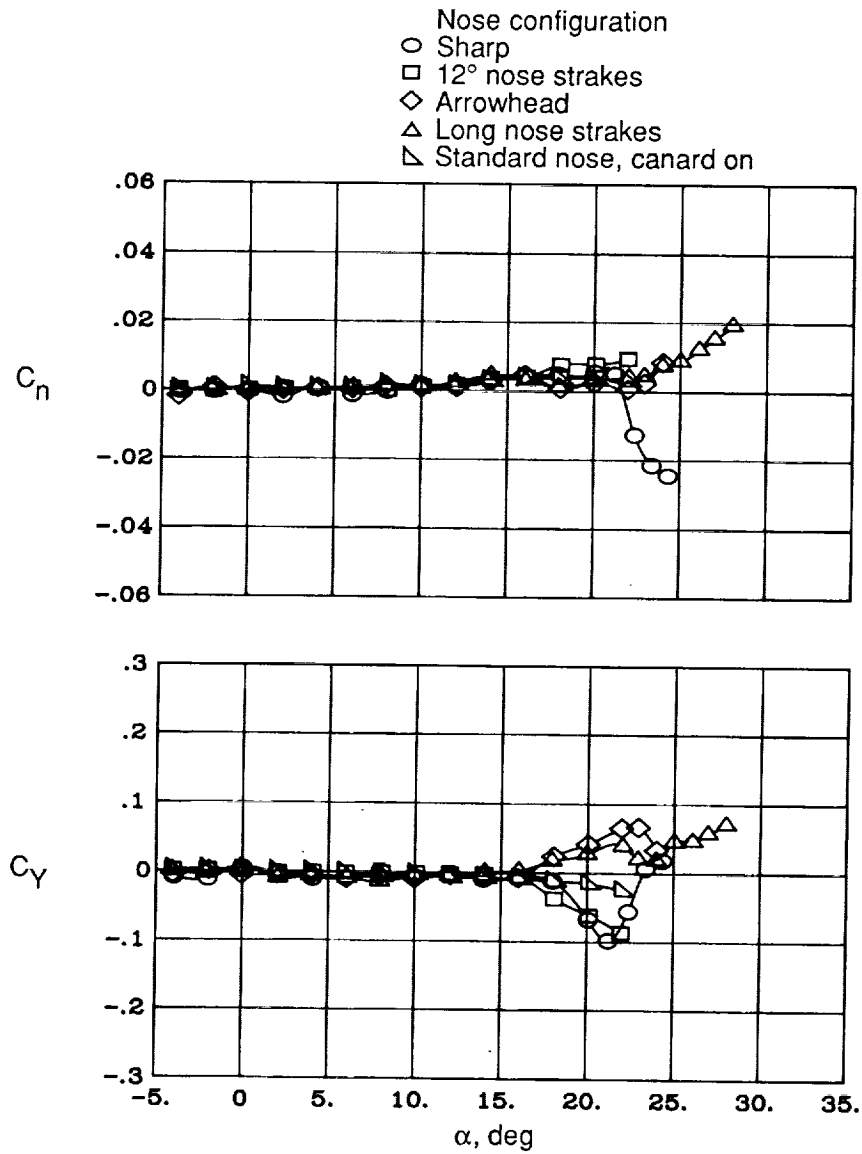
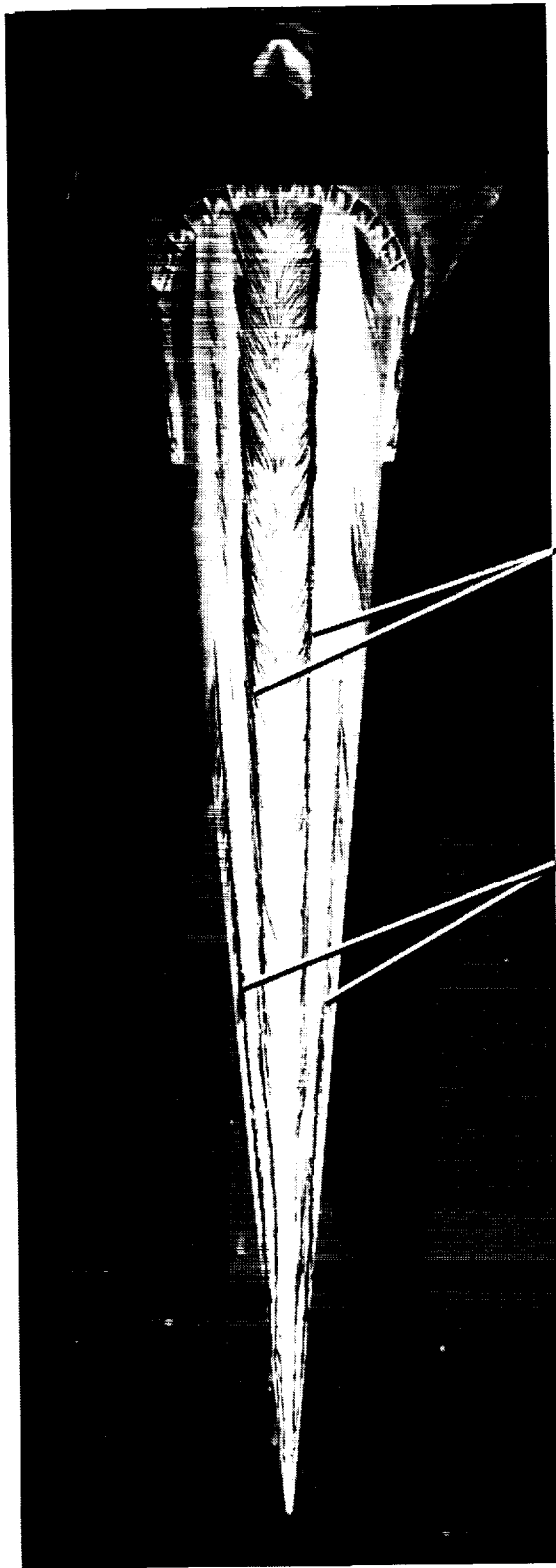


Figure 19. Effects of nose geometry on directional data. 6° cone forebody; B, W, F, T;  $C_T = 0$ .





Vortex flow secondary  
separation lines

Vortex flow primary  
separation lines

L-89-119

(a) Top view.

Figure 20. Surface oil flow visualization for 6° cone forebody configuration with standard nose. B, W, F, T;  
 $\alpha = 16^\circ$ ;  $C_T = 0$ .

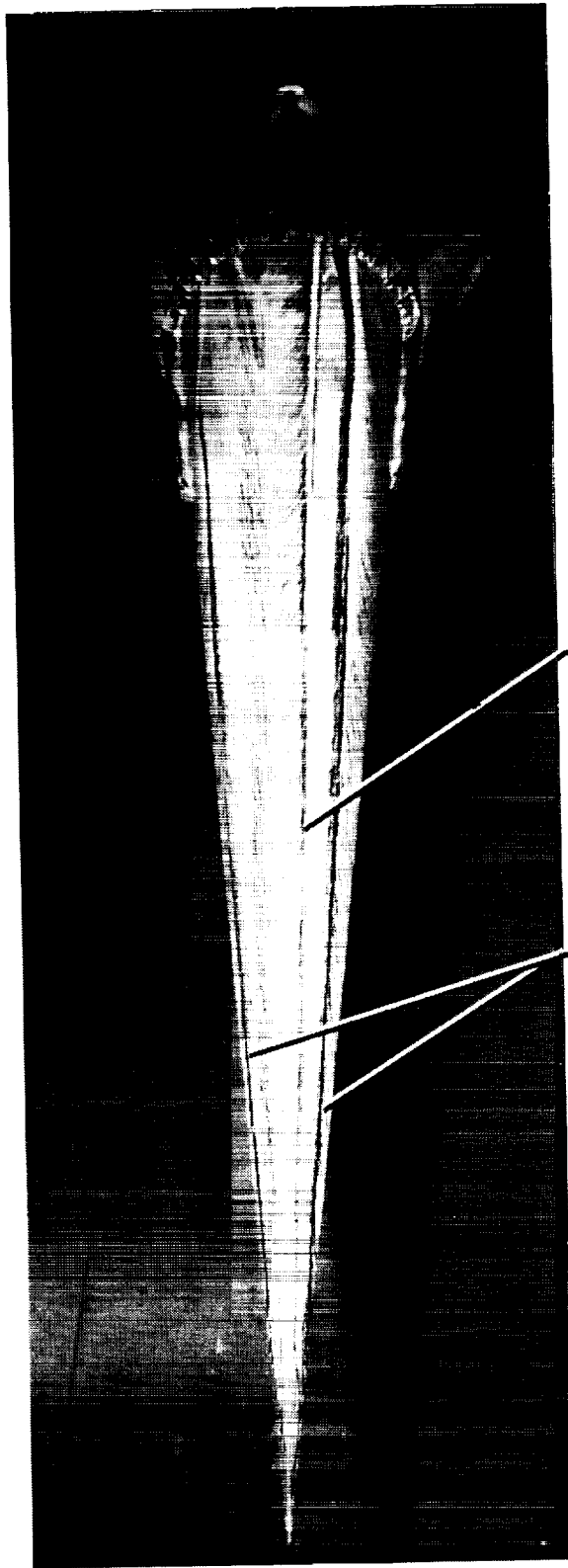


L-88-6546

(b) Side view.

Figure 20. Concluded.

ORIGINAL PAGE  
BLACK AND WHITE PHOTOGRAPH

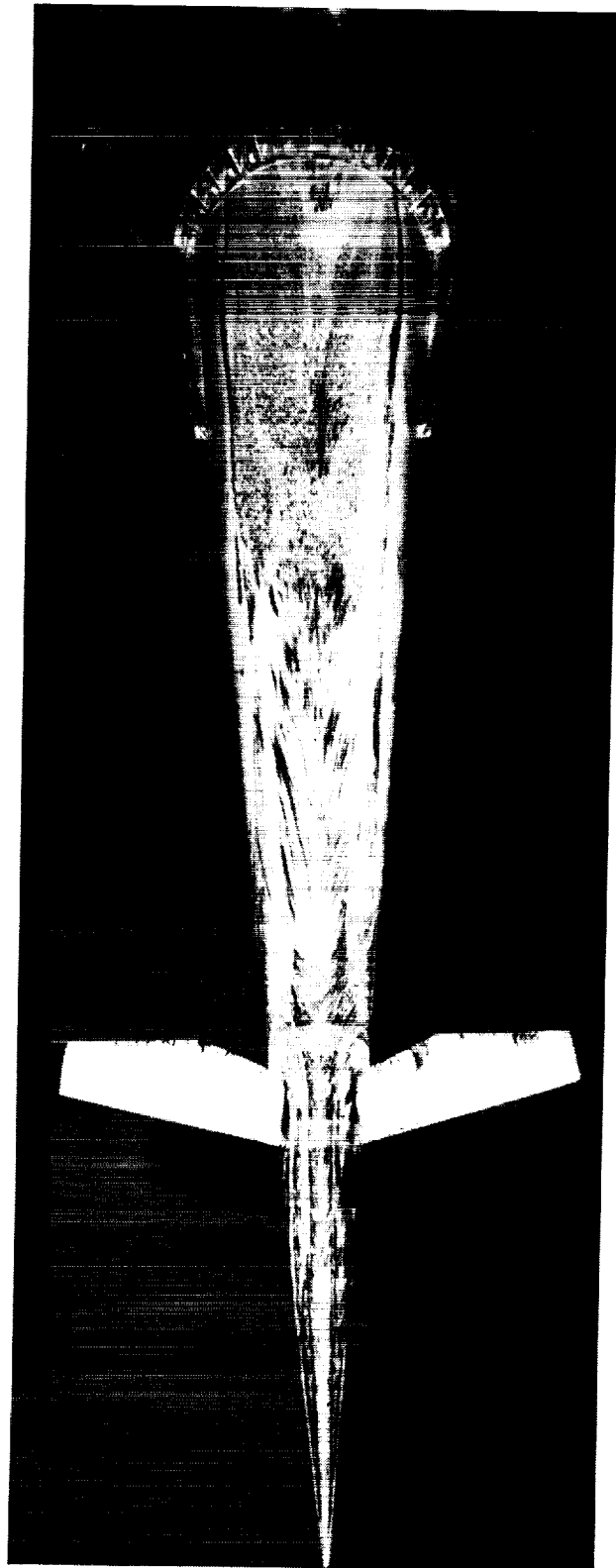


Vortex flow secondary  
separation line

Vortex flow primary  
separation lines

L-89-120

Figure 21. Surface oil flow visualization for 6° cone forebody configuration with sharp nose. B, W, F, T;  
 $\alpha = 18^\circ$ ;  $C_T = 0$ .

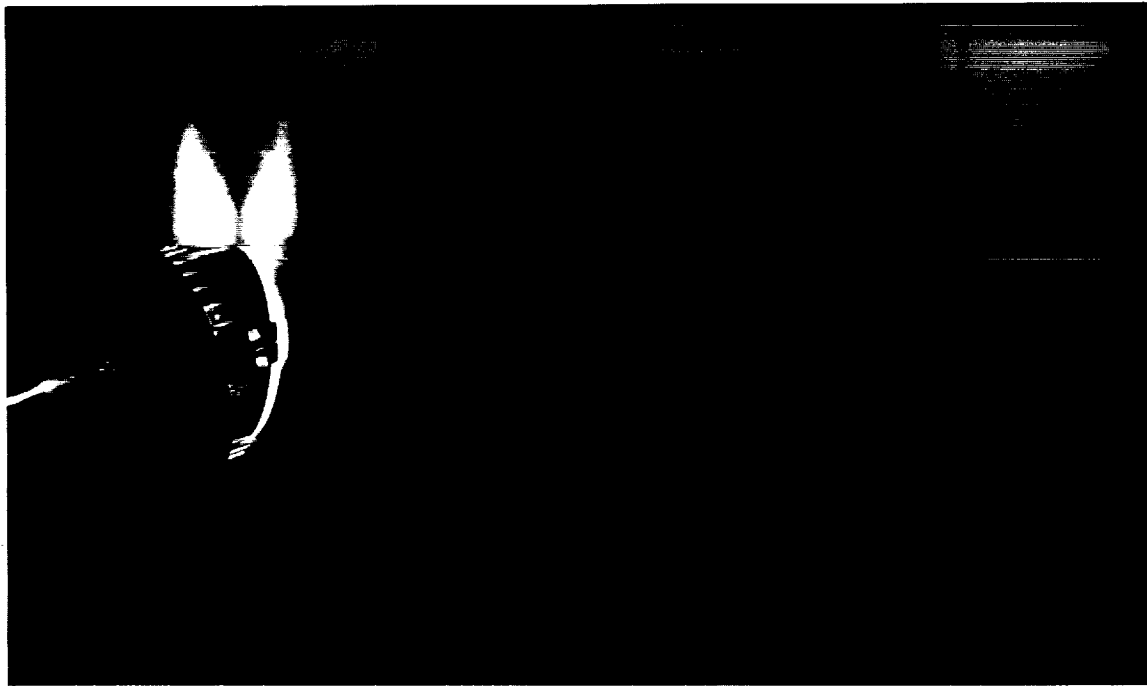


L-89-121

Figure 22. Surface oil flow visualization for 6° cone forebody configuration with standard nose and canard on.  
B, W, F, T;  $\alpha = 16^\circ$ ;  $C_T = 0$ .



(a) Canard off.



(b) Canard on.

L-89-122

Figure 23. Off-surface flow visualization using smoke and laser light sheet. 6° cone forebody; B, W, F, T;  
 $\alpha = 16^\circ$ ;  $C_T = 0$ ;  $q_\infty = 3.4$  psf.

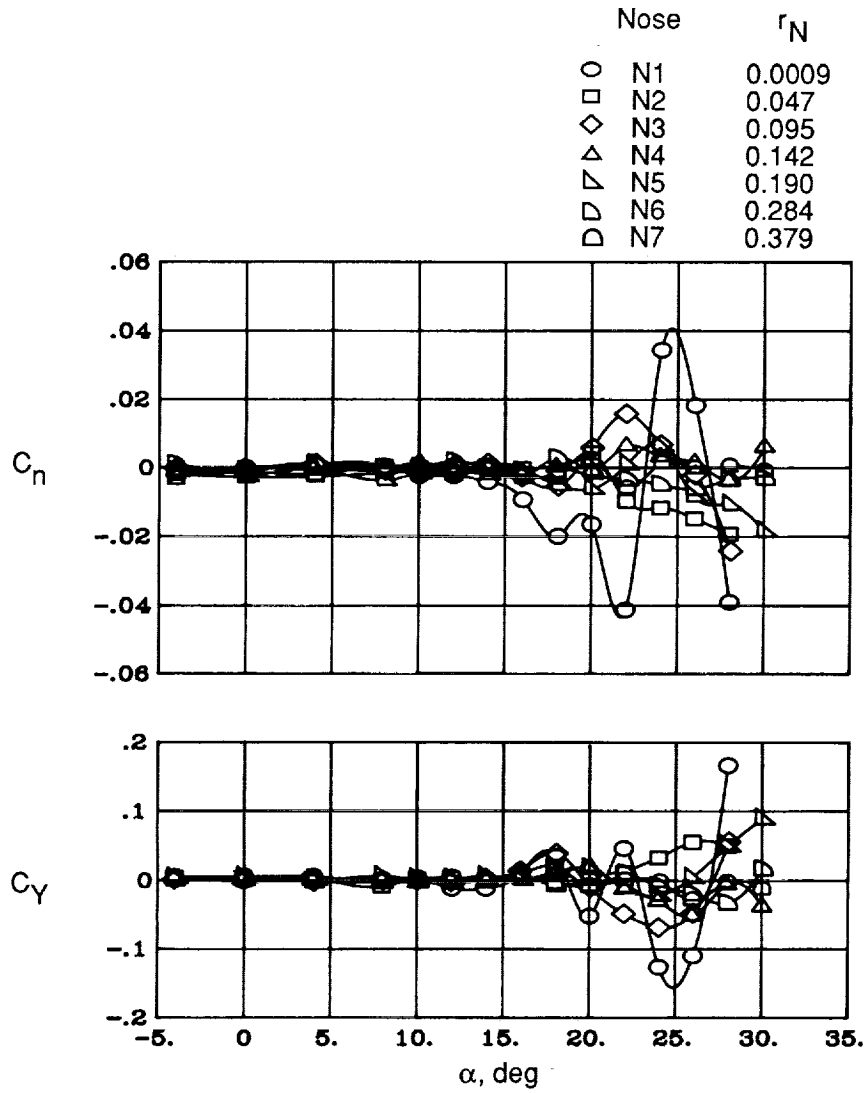


Figure 24. Effects of nose bluntness on directional data.  $5^\circ$  cone forebody; body alone;  $C_T = 0$ .

Nose	$r_N$
○ N1	0.0009
□ N3	0.095
◇ N5	0.190
△ N7	0.379

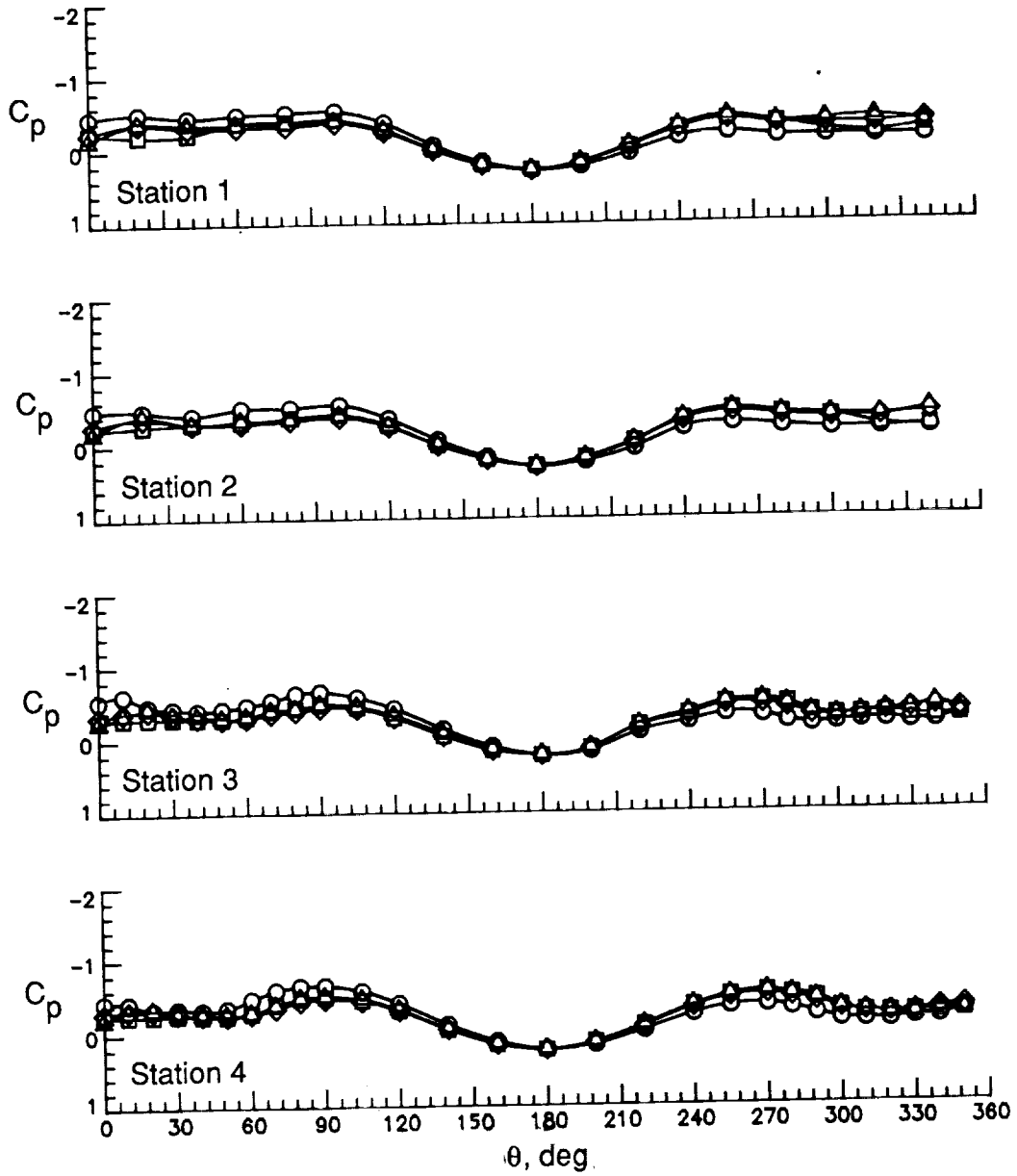


Figure 25. Forebody pressure data illustrating the effects of nose bluntness.  $5^\circ$  cone forebody; body alone;  $\alpha = 24^\circ$ ;  $C_T = 0$ .

	Nose	$r_N$
○	N1	0.0009
□	N3	0.095
◇	N5	0.190
△	N7	0.379

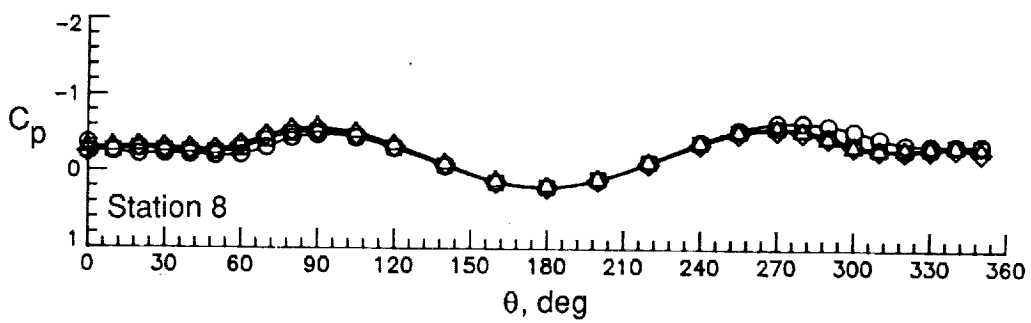
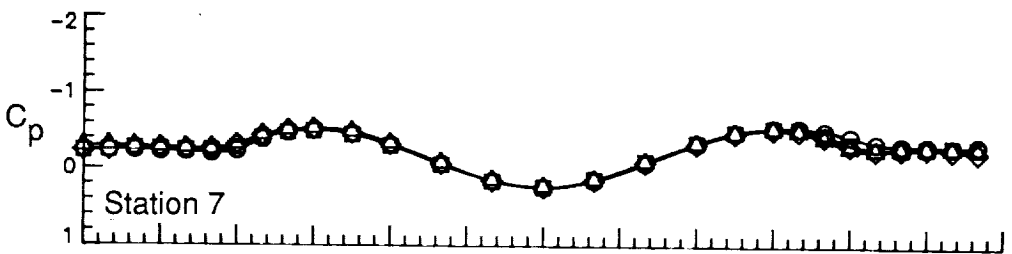
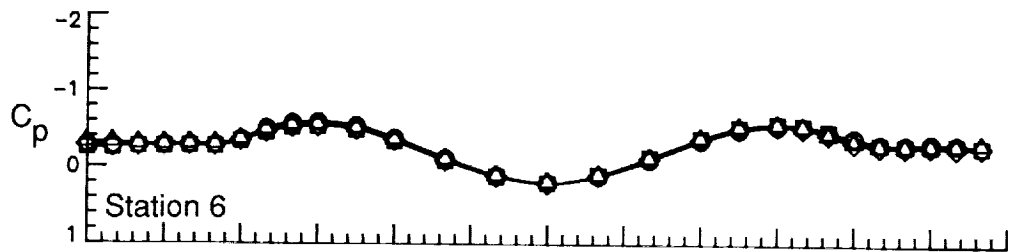
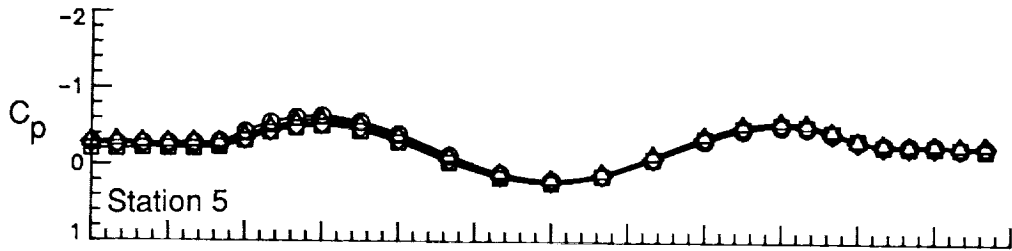


Figure 25. Continued.



	Nose	$r_N$
○	N1	0.0009
□	N3	0.095
◇	N5	0.190
△	N7	0.379

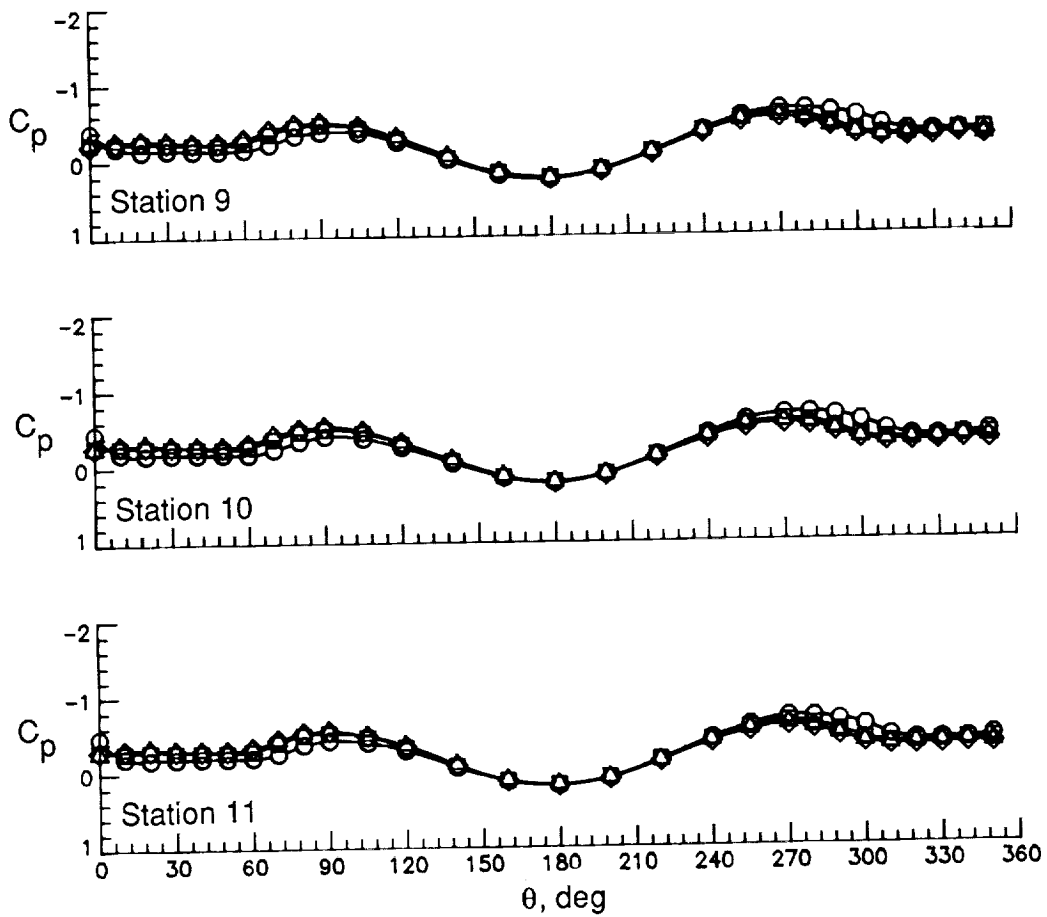


Figure 25. Concluded.

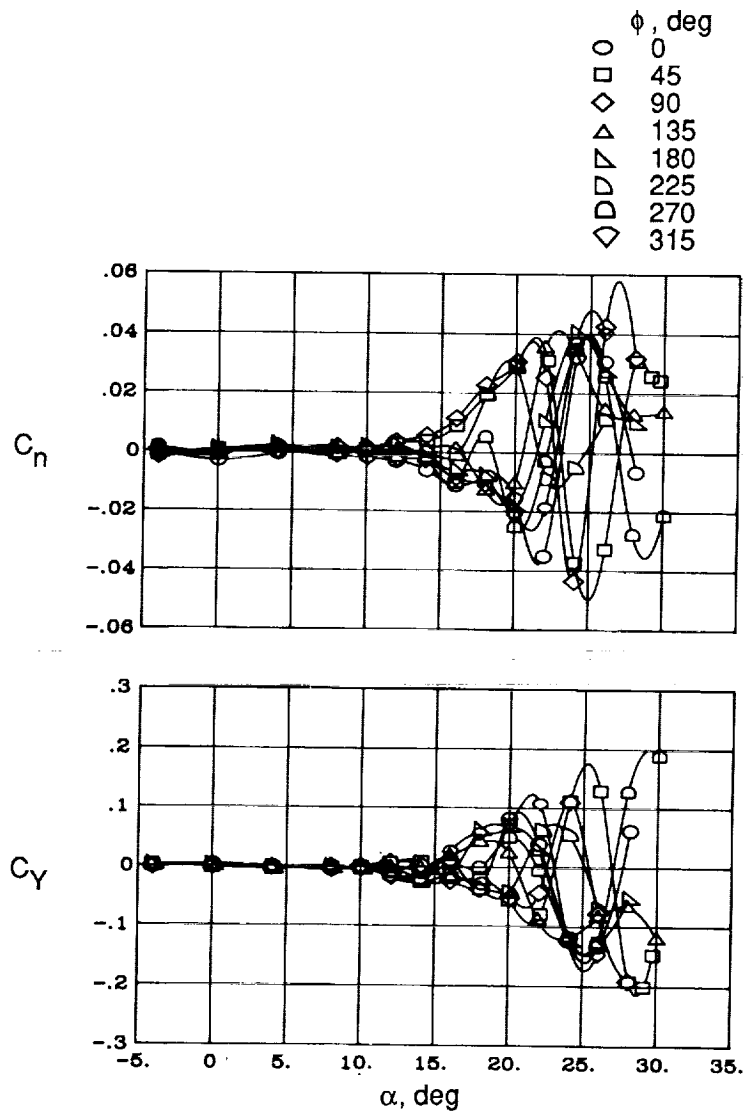


Figure 26. Effects of sharp nose rotation angle on directional data.  $5^\circ$  cone forebody; body alone;  $C_T = 0$ .

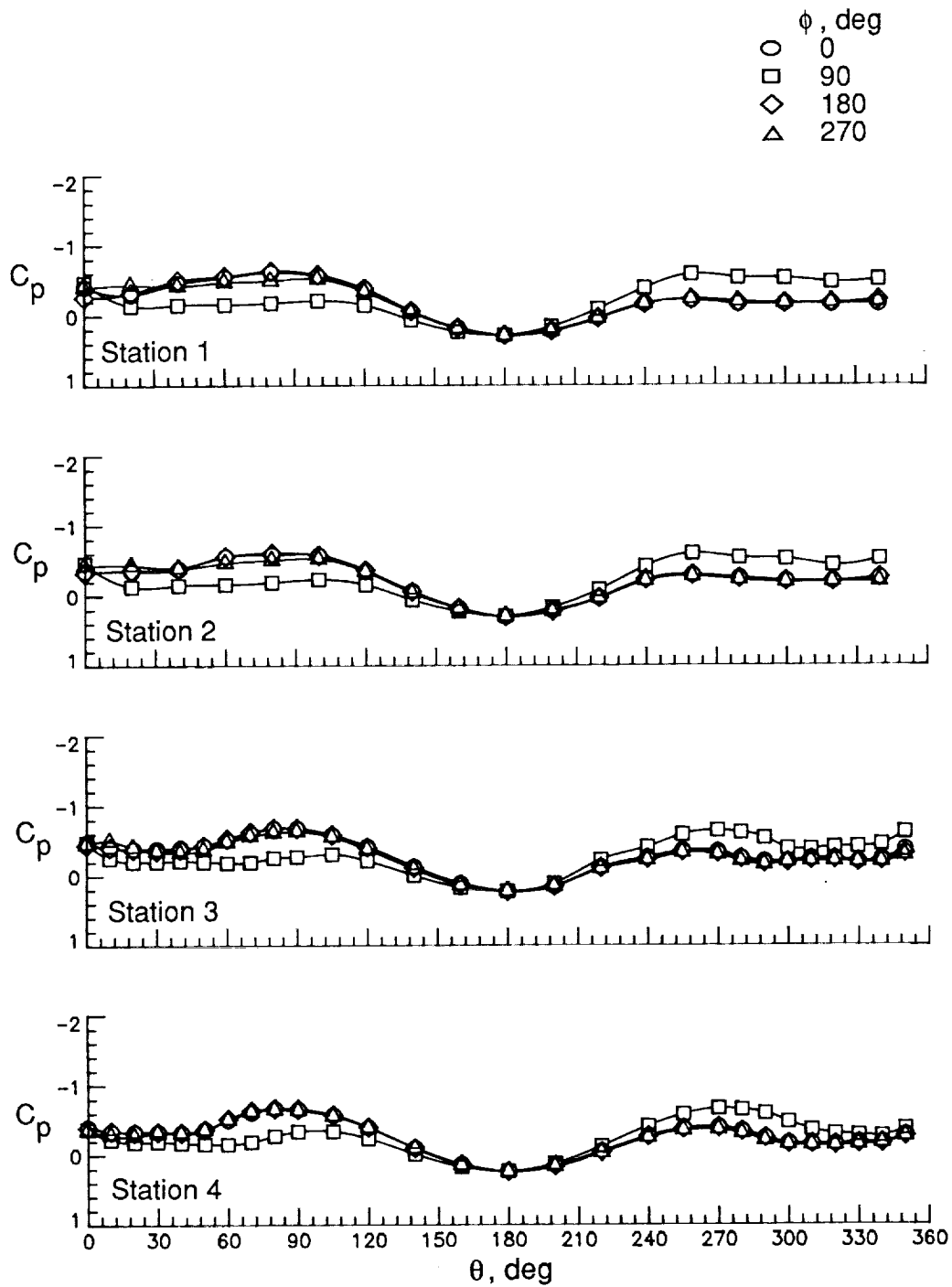


Figure 27. Forebody pressure data illustrating effects of sharp nose rotation angle.  $5^\circ$  cone forebody; body alone;  $\alpha = 24^\circ$ ;  $C_T = 0$ .

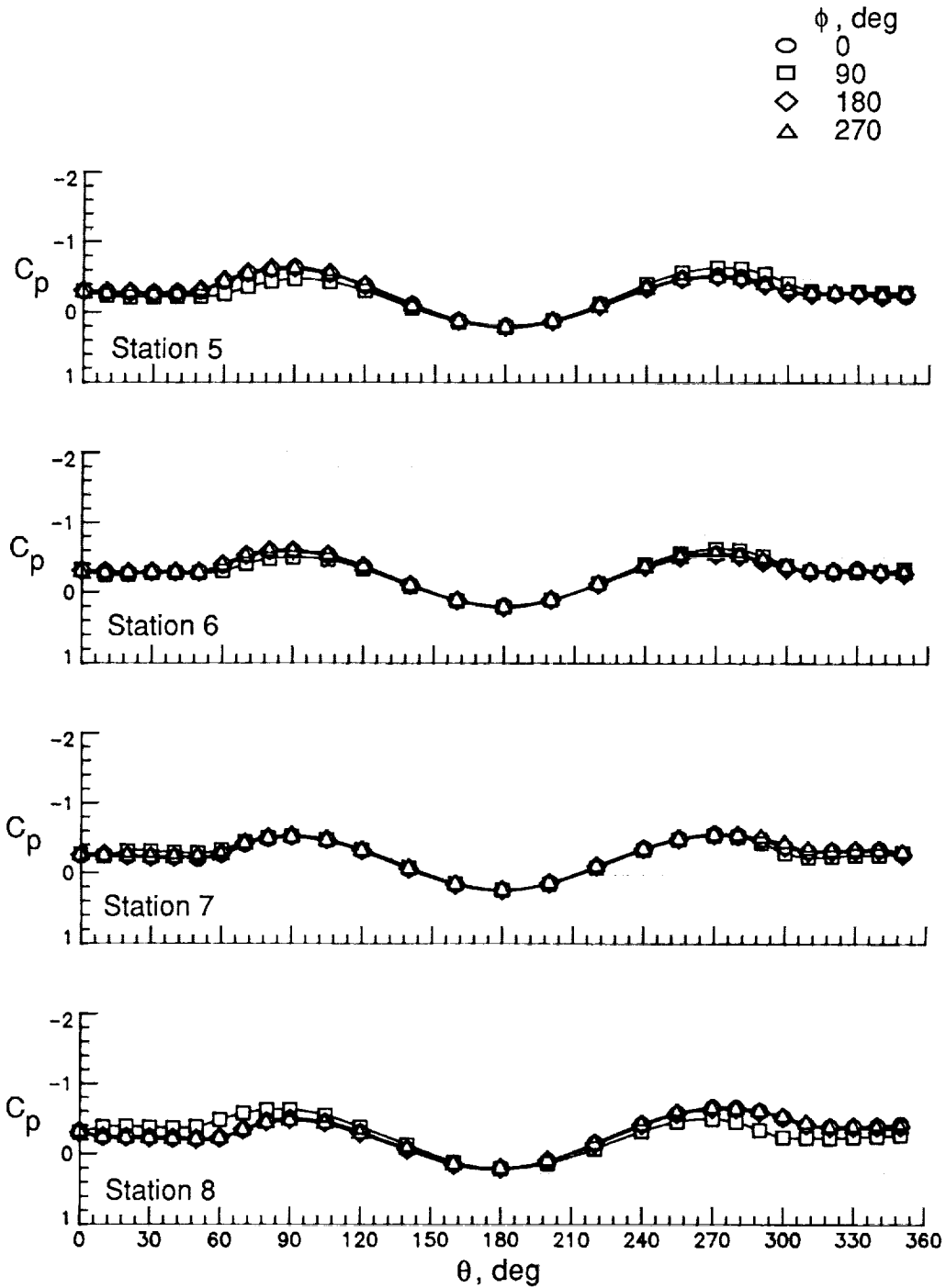


Figure 27. Continued.

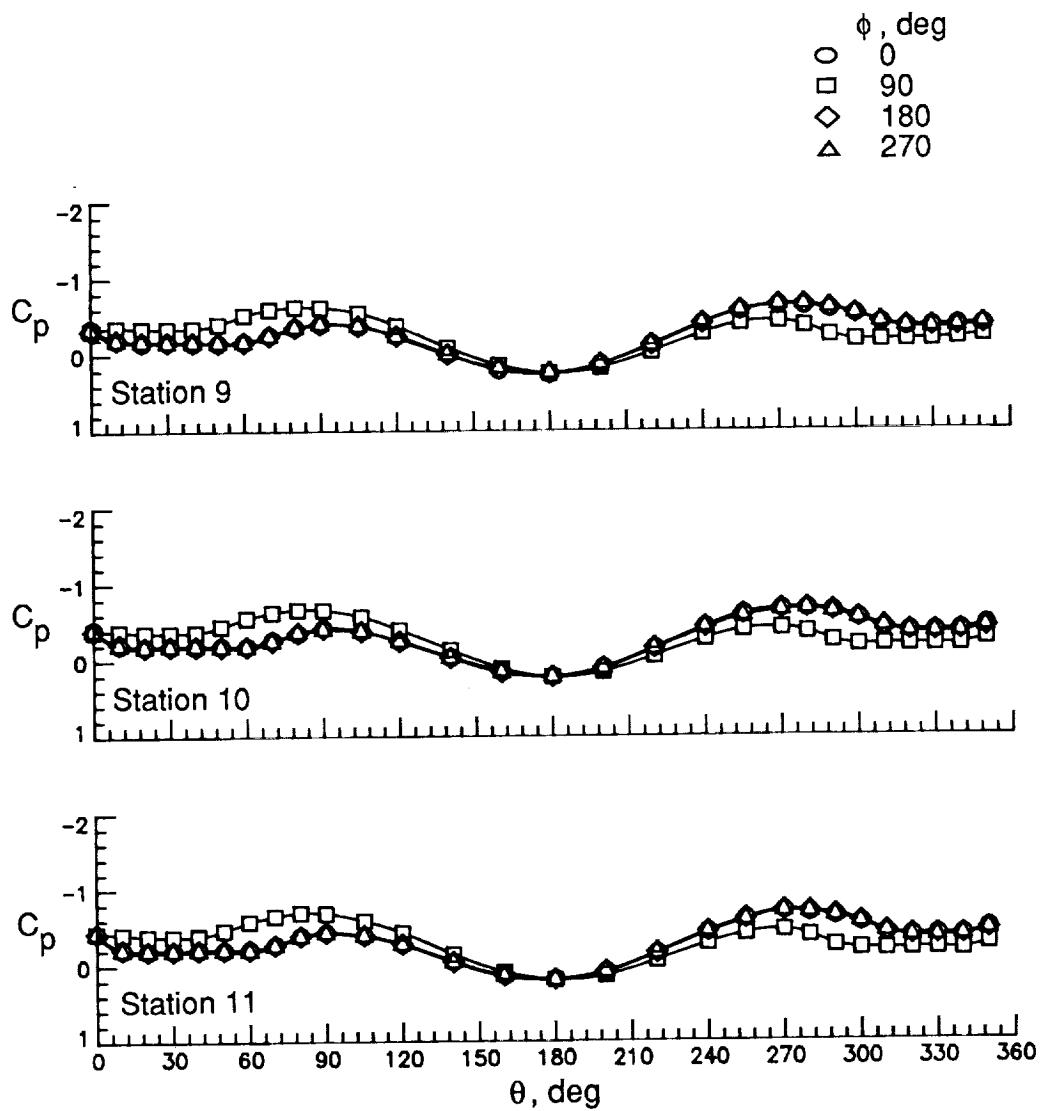


Figure 27. Concluded.

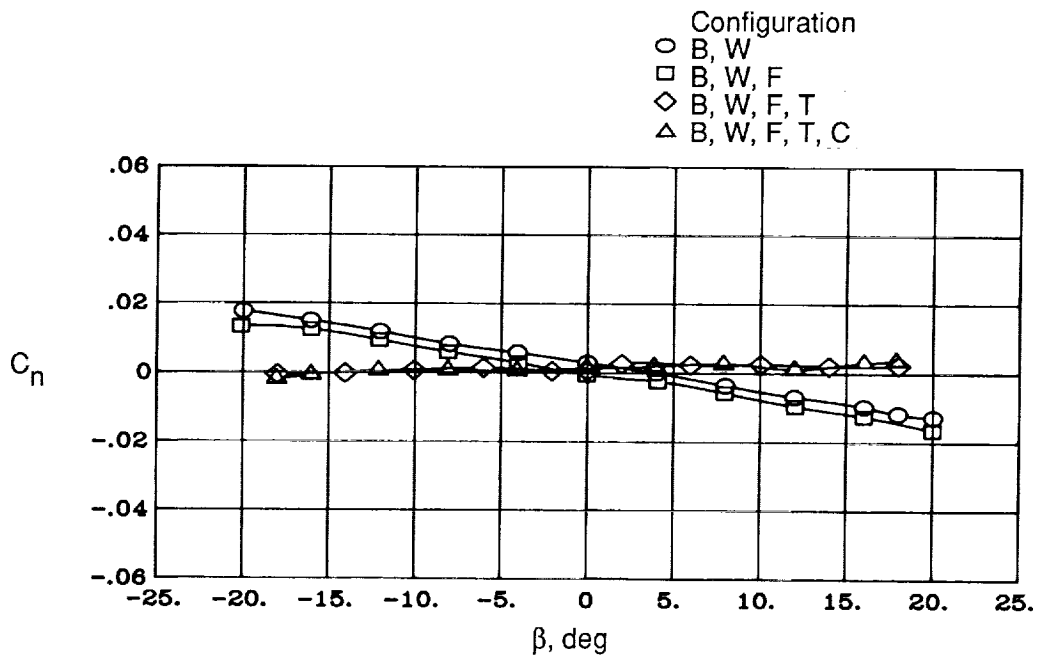


Figure 28. Effects of configuration buildup on directional stability.  $6^\circ$  cone forebody;  $\alpha = 8^\circ$ ;  $C_T = 0$ .

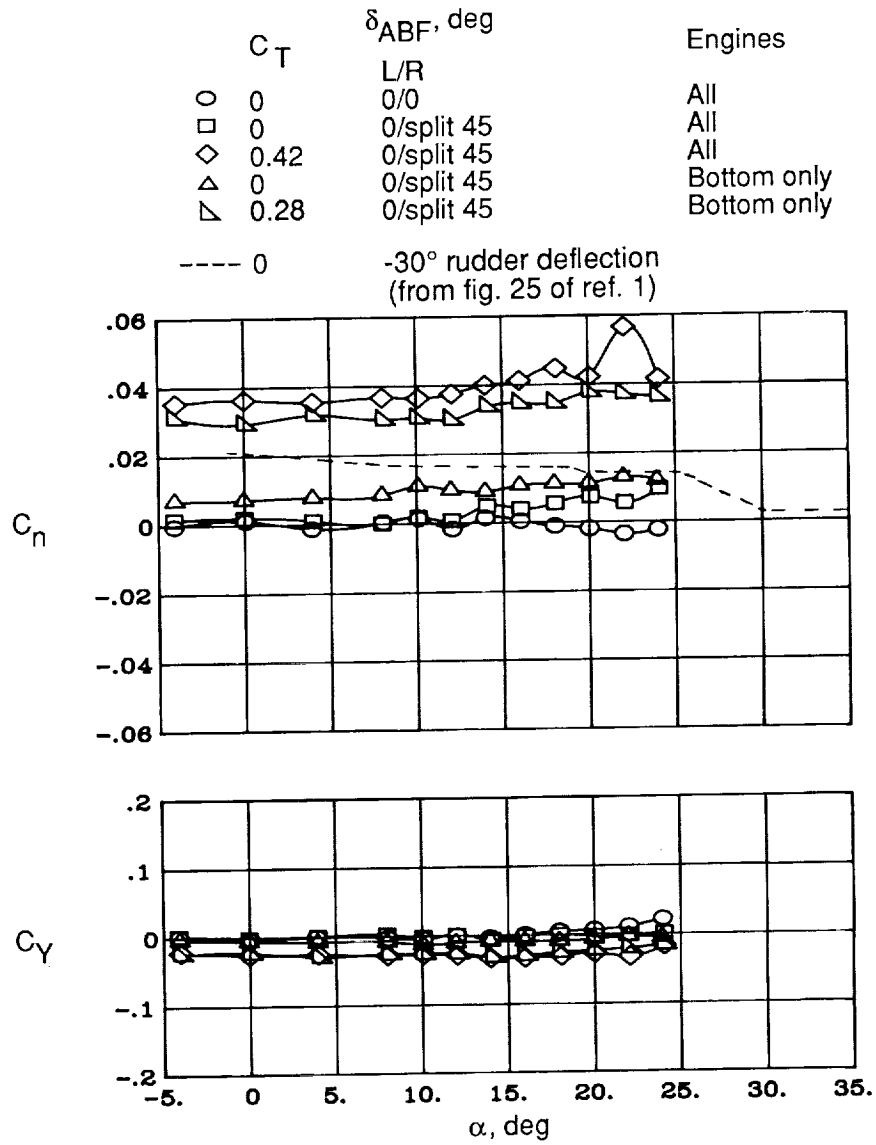
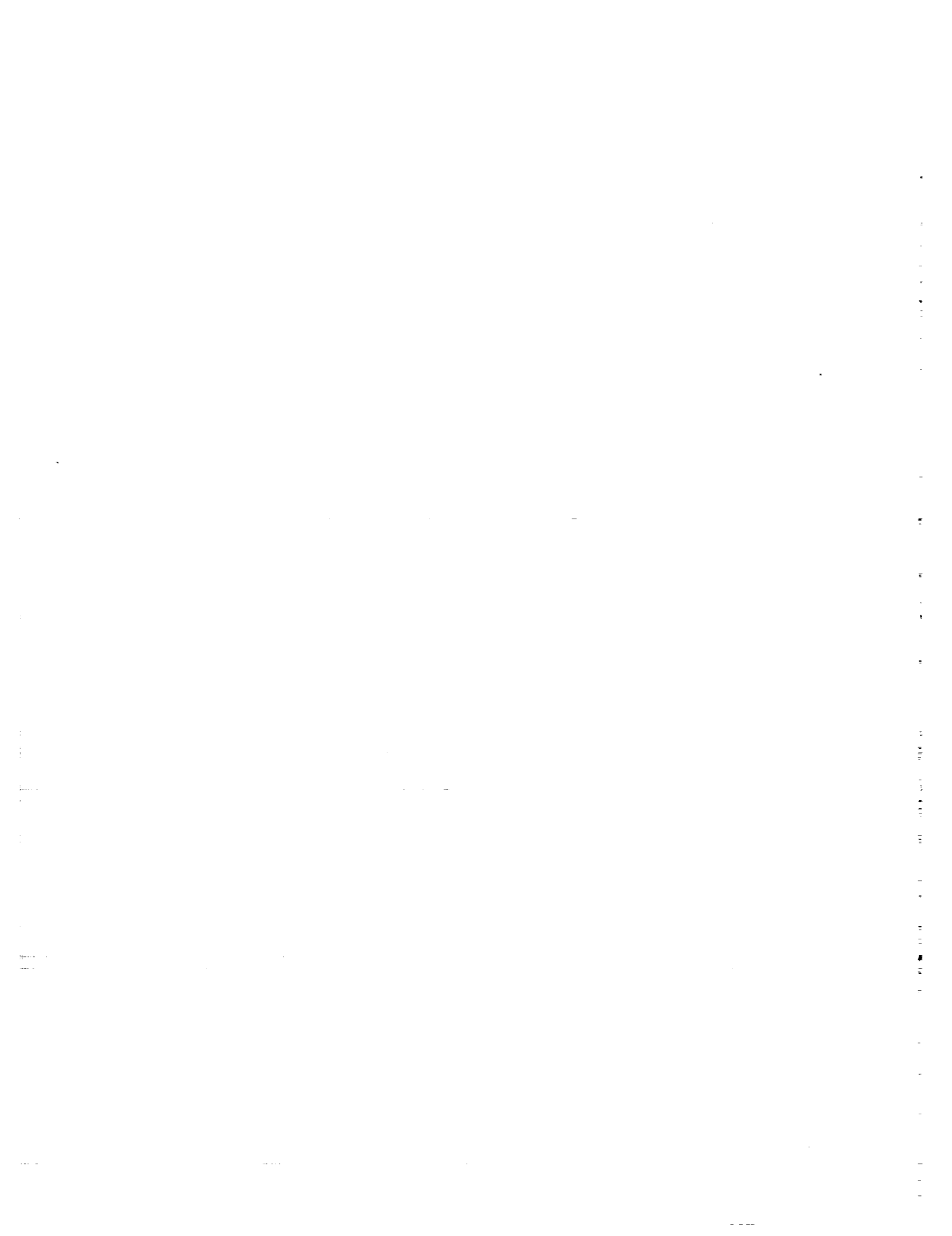


Figure 29. Split flap effectiveness for all engines and bottom engines only. 5° cone forebody; B, W, LS, SC, ABF;  $\delta_f = 0^\circ$ .







## Report Documentation Page

1. Report No. NASA TP-2945		2. Government Accession No.		3. Recipient's Catalog No.	
4. Title and Subtitle Low-Speed, High-Lift Aerodynamic Characteristics of Slender, Hypersonic Accelerator-Type Configurations				5. Report Date November 1989	
				6. Performing Organization Code	
7. Author(s) Gregory M. Gatlin				8. Performing Organization Report No. L-16537	
9. Performing Organization Name and Address NASA Langley Research Center Hampton, VA 23665-5225				10. Work Unit No. 763-01-31-22	
				11. Contract or Grant No.	
12. Sponsoring Agency Name and Address National Aeronautics and Space Administration Washington, DC 20546-0001				13. Type of Report and Period Covered Technical Paper	
				14. Sponsoring Agency Code	
15. Supplementary Notes					
16. Abstract Two investigations were conducted in the Langley 14- by 22-Foot Subsonic Tunnel to determine the low-speed aerodynamic characteristics of a generic hypersonic accelerator-type configuration. The model was a delta wing configuration incorporating a conical forebody, a simulated wrap-around engine package, and a truncated conical afterbody. Six-component force and moment data were obtained over a range of angle of attack from $-4^\circ$ to $30^\circ$ and a range of sideslip from $-20^\circ$ to $20^\circ$ . In addition to tests of the basic configuration, component buildup tests were conducted, and the effects of power, forebody nose geometry, canard surfaces, fuselage strakes, and engines on the lower surface alone were also determined. Control power available from deflections of wing flaps and afterbody flaps was also investigated and found to be significantly increased during power-on conditions. Large yawing moments resulted from asymmetric flow fields exhibited by the forebody as revealed by both surface pressure data and flow visualization. Increasing nose bluntness reduced the yawing-moment asymmetry, and the addition of a canard eliminated the yawing-moment asymmetry.					
17. Key Words (Suggested by Authors(s)) Conical aerospace plane Flow visualization Control power Vortex flow Low speed			18. Distribution Statement Unclassified—Unlimited  Subject Category 02		
19. Security Classif. (of this report) Unclassified		20. Security Classif. (of this page) Unclassified		21. No. of Pages 44	22. Price A03

